

Josephson parametric reflection amplifier with integrated directionality

M. P. Westig* and T. M. Klapwijk†

Kavli Institute of NanoScience, Delft University of Technology, Lorentzweg 1, 2628 CJ Delft, The Netherlands

(Dated: May 22, 2018)

A directional superconducting parametric amplifier in the GHz frequency range is designed and analyzed, suitable for low-power read-out of microwave kinetic inductance detectors employed in astrophysics and when combined with a nonreciprocal device at its input also for circuit quantum electrodynamics (cQED). It consists of an one wavelength long nondegenerate Josephson parametric reflection amplifier circuit. The device has two Josephson junction oscillators, connected via a tailored impedance to an on-chip passive circuit which directs the in- to the output port. The amplifier provides a gain of 20 dB over a bandwidth of 220 MHz on the signal as well as on the idler portion of the amplified input and the total photon shot noise referred to the input corresponds to maximally ~ 1.3 photons per second per Hertz of bandwidth. We predict a factor of four increase in dynamic range compared to conventional Josephson parametric amplifiers.

I. INTRODUCTION

Nonlinearities in superconducting devices, such as the nonlinear Josephson inductance [1], are building blocks for parametric amplification. They can be employed in low noise Kerr-type nonlinear oscillators, providing three- or four-wave mixing interactions [2, 3] enabling degenerate (phase sensitive) or nondegenerate (phase preserving) operation [4]. In this letter we design and analyze such a parametric amplifier with integrated directionality, facilitating emerging low-power read-out schemes for microwave kinetic inductance microresonator detectors (MKID) [5, 6] employed in astrophysics instruments. While our amplifier concept is directional although reciprocal, it is only one wavelength long which suits and further integrates the MKID read-out backend. Recent findings suggest that the vacuum noise generated at the input of our parametric amplifier does not decrease the sensitivity of the MKID. State-of-the-art read-out schemes of this detector use read-out photon numbers of many hundreds of millions in order to overcome the cryogenic high electron-mobility amplifier noise and often no circulators are used between the detector and the read-out amplifier [5]. It is expected, however, that the MKID sensitivity can be further increased by reducing the read-out photon number which can be achieved by parametric amplifiers [6] such as Josephson parametric amplifiers (JPA). Eventually this will help to uncover fundamental sources of two-level system noise in superconducting microresonators of which no microscopic theory yet exists, important for detectors but also for quantum information processors. In order to be practicable in view of the complete detection instrument, maybe first in small arrays of about hundred MKID detectors, the amplifier bandwidth has to be several tens of a MHz large, the dynamic range should enable to process first up to on average 100 read-out photons and the amplifier should be directional, compact in size and easy to fabricate.

A second application of our amplifier could be in a circuit quantum electrodynamics (cQED) [7–14] measurement scheme. In this case our amplifier would have to be supplemented by a nonreciprocal device at its input to filter out the vacuum noise that would otherwise increase the parasitic photon population of a quantum sensitive device connected to the input. Also, few other parasitic photons could arise at the input of the parametric amplifier due to a finite return loss of the amplifier. Research on novel nonreciprocal device technologies without lossy and possibly disturbing magnetic materials, is presently an active field and is expected to provide adequate solutions soon. Here, techniques are employed from cavity optomechanics [15–22] over emulation of circulators with parametric active devices [23] or with Wheatstone bridge-based superconducting LC resonators [24, 25]. Also, innovative techniques in cQED [26–30] and different Josephson parametric converter circuits [31–33] as well as other directional Josephson circuits [34, 35] have been realized. Together with the integrated directionality of our amplifier, it is very likely that the parasitic photon population of a quantum sensitive device connected to the nonreciprocal device-parametric amplifier combination is effectively reduced. The nonreciprocal device would have to filter out only the vacuum noise and not direct additionally the amplified field to the measurement chain which is separately achieved by our amplifier concept.

II. AMPLIFIER DESIGN AND PERFORMANCE

A. General Concept

Our amplifier is operated close to its bifurcation point when the dynamics are that of a Duffing oscillator, a small input signal change induces a large variation in the system dynamics leading to amplification [36–39].

Figure 1(a) shows the aluminum microstrip circuit of the JPA. Essential elements are a superconducting branch-line coupler (like we have realized experimentally in Refs. [40, 41]) and an embedding circuit which is con-

* m.p.westig@tudelft.nl

† t.m.klapwijk@tudelft.nl

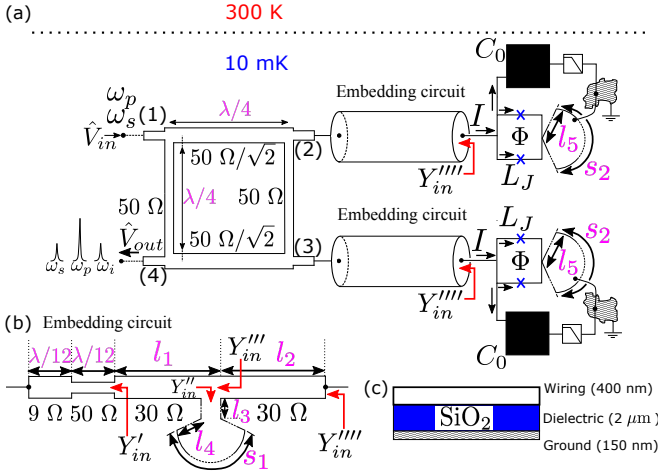


FIG. 1. **JPA with directionality.** (a) Top view on the 400 nm wiring of the aluminum microstrip circuit, consisting of three essential elements; branch-line coupler with ports (1) to (4), embedding circuit and Josephson junction oscillators with inductance L_J (crosses) and capacitance C_0 . A signal \hat{V}_{in} having frequency ω_s and injected in (1) along with a strong pump tone of frequency ω_p is amplified and directed to (4). Additionally, amplified vacuum noise is emitted from input port (1) because of the reciprocity of the device. Also, few other parasitic photons could arise at the input due to a finite return loss of the amplifier. (b) Details of the embedding circuit of the best performance JPA[-0.36,+0.36], c.f. Table I. (c) Cross-section of microstrip layers.

ected to two individual *rf*-shunted nonlinear Josephson junction oscillators (JJO), operated at ~ 10 mK. The branch-line coupler combines the individual JJOs to a single JPA [42] and provides signal directivity while the matched input admittance Y_{in}'''' of the embedding circuit determines gain, noise and bandwidth of the JPA via its engineered conductance and susceptance portions. The value of Y_{in}'''' is dominated by a capacitive shunt of the first $\lambda/12$ section in the embedding circuit rather than by a higher impedance inductive load like realized in earlier work [43, 44].

Each of the two JJOs should be characterized by the same plasma frequency $\omega_0 = ((2\pi I_c(\Phi))/(\phi_0 C_0))^{-1/2}$. Here, $L_J(\Phi) = \phi_0/(2\pi I_c(\Phi))$ is the Josephson inductance being 0.12 nH in our case and $C_0 = 4.0$ pF is the shunting capacitor. Furthermore, $\phi_0 = h/(2e)$ is the flux quantum and $I_c(\Phi) = 2i_c |\cos(\pi\Phi/\phi_0)|$ is the total critical current for each Josephson SQUID shown in Fig. 1(a) with i_c being the individual currents of the single junctions in the SQUID. An externally applied small magnetic flux bias induced in the SQUID loop, Φ , tunes $\omega_0/(2\pi) \sim 7.3$ GHz and the JJO admittance $Y_0 = \sqrt{C_0/L_J(\Phi)}$. The JJOs are pumped through their embedding circuit by a strong coherent tone of frequency $\omega_p/(2\pi) \sim 6.0$ GHz which provides the energy for the amplification and by a much weaker quantum signal of frequency ω_s which shall be amplified. In this work we consider nondegenerate four-wave mixing as amplifying

TABLE I. Three JPA designs resulting in different residual frequency dependent imaginary parts in $-i\tilde{\omega}_s + \kappa[\tilde{\omega}_s]/2 \propto Y_{in}''''[\tilde{\omega}_s]$ of Eq. (2). We quantify the residue by indicating the minimum/maximum slope of the imaginary part as index, e.g. JPA[-0.36,+0.36]. A weakly frequency dependent imaginary part with a slope symmetric around zero yields a maximal bandwidth determined by $\text{Re}[Y_{in}''''[\tilde{\omega}_s]]$. The numbers specify the dimensions of the circuit parts in μm from which the characteristic impedance in Ω is given in curly brackets.

Elements	JPA[-1,+1]	JPA[-0.36,+0.36]	JPA[-0.53,-0.19]
$\lambda/4$ [(1)-(2)] ^a	7098 {50/ $\sqrt{2}$ }	7098 {50/ $\sqrt{2}$ }	7098 {50/ $\sqrt{2}$ }
$\lambda/4$ [(1)-(4)] ^b	7306 {50}	7306 {50}	7306 {50}
$\lambda/12$ [1st]	1177 {5}	1522 {9}	1941 {16}
$\lambda/12$ [2nd]	1332 {50}	1722 {50}	2077 {50}
l_1	1587 {30}	2137 {30}	2650 {30}
l_2	8815 {30}	9515 {30}	10262 {30}
l_3	262 {30}	182 {30}	182 {30}
l_4	290	224	155
s_1	658	553	422
l_5	2598	2598	2598
s_2	4848	4848	4848

^a The connection of ports (3) and (4) has the same length.

^b The connection of ports (2) and (3) has the same length.

mechanism for which $2\omega_p = \omega_s + \omega_i$; two pump photons at ω_p transfer their energy into signal and idler modes symmetric around ω_p , c.f. Fig 1(a). The Josephson SQUIDs are designed on top of a 2 μm thick SiO_2 dielectric layer, c.f. Fig. 1(c). Each of the SQUIDs is *rf*-shunted through a virtual short around 6 GHz, realized by a broadband radial stub tuner [45] with dimensions $\{s_2, l_5\}$ and characteristic input impedance of 50 Ω . A bonding wire connects the edge of the radial stub directly to an island on the ground plane, connecting the otherwise galvanically separated microstrip layers. On the other side of the SQUID, the same island connects to a planar low pass filter (e.g. a standard microstrip Chebyshev *rf*-blocking filter [46]), being connected to the oscillator's shunting capacitor C_0 . Therefore, a *dc*-current can flow through the SQUID, providing the inductance L_J , and at the same time the bonding wires do not disturb the *rf* circuit.

B. Equation of Motion, Gain and Noise

The equation of motion (EOM) for each of the two JJOs is described by independent Duffing equations obtained from the RCSJ-model [47] and by *Kirchhoff's* law applied to the equivalent circuit of the JJO and its embedding circuit, shown in Fig. 1(a) and (b):

$$\ddot{\delta}(t) + \kappa\dot{\delta}(t) + \omega_0^2 \left[\delta(t) - \frac{\delta(t)^3}{6} \right] - \omega_0^2 \frac{I_p(t)}{I_c(\Phi)} = \frac{4\pi\hat{I}_{in}(t)}{\phi_0 C_0}. \quad (1)$$

This equivalent circuit describes the pumping of the particular JJO from a (parallel) current source with admittance Y_{in}'''' . Furthermore, $\delta(t) = \delta_p(t) + \hat{\delta}_s(t)$ is

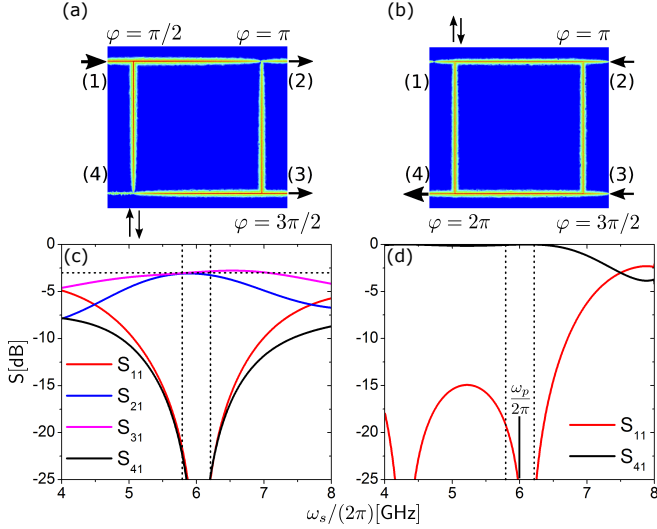


FIG. 2. **Directionality.** (a) and (b) show a snapshot of $|\mathbf{E}(\mathbf{r})|$ on the branch-line coupler at the design frequency 6 GHz. (c) and (d) quantify the corresponding scattering parameters, determining a slight asymmetry in the coupler performance. Note that in (d) the scattering parameters are fully reciprocal, in particular $S_{41} = S_{14}$. Hence, vacuum noise is generated at input port (1). In applications for cQED this noise has to be filtered out by an additional nonreciprocal device connected to input port (1). (a) Excitation of port (1) and phase distribution to ports (2) and (3) connecting to the amplifier circuits (not shown); port 4 receives no signal and this is indicated by the up-down arrows illustrating an out-of-phase condition. (b) Returning phase delayed signals from the amplifier circuits, combining this time in-phase at the output port (4) and not at port (1), quantified by the value S_{11} . In (b) the gain is set to $G = 1$ for illustrative purposes. Vertical dashed lines are taken from Fig. 4(b) indicative of the amplifier -3 dB bandwidth and the horizontal dashed line is the -3 dB level of the branch-line coupler.

the intra-oscillator field and consists of a classical term $\delta_p(t)$ due to the coherent large amplitude pump tone, $I_p(t) = \bar{I}_p \cos(\omega_p t)$, and a quantum term $\hat{\delta}_s(t)$ induced by the weak signal $\hat{I}_{in}(t)$. The dissipation is quantified by a rate $\text{Re}[\kappa] = \text{Re}[Y_{in}'''']/C_0$, obtaining the convenient value $\text{Re}[\kappa]/(2\pi) \sim 1.33$ GHz. Equation (1) only holds for a strong nonlinearity of the JJO compared to the linear inductance L_{env} contributed by the embedding circuit. This is quantified by the participation ratio $p = L_{\parallel}/L_J$ [39] and $L_{\parallel}^{-1} = L_{env}^{-1} + L_J^{-1}$ where L_{\parallel} is the total parallel inductance. We find that L_{env} is larger by about a factor 22 compared to L_J so that the nonlinearity of the JJO is strong enough to assume the ideal case provided by Eq. (1), where the nonlinear term reads $p\delta(t)^3/6 \approx \delta(t)^3/6$. For $\hat{I}_{in} = 0$, one obtains the steady state solution of Eq. (1) which determines the classical pump intra-oscillator field $\delta_p(t)$ with maximum amplitude $\delta_{p,max}$.

The case $\hat{I}_{in} \neq 0$ obtains the quantum intra-oscillator field by subtracting the steady state solution from

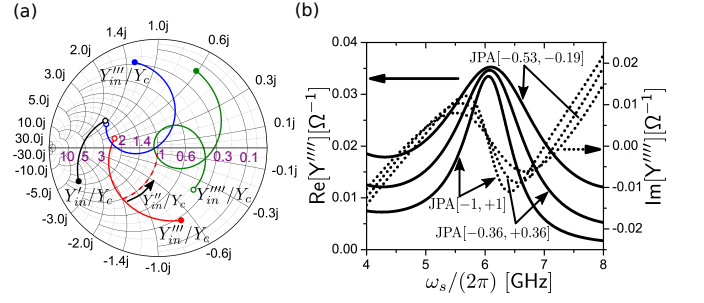


FIG. 3. **Embedding circuit design.** (a) The Smith chart shows the design relevant input admittances in the polar plane, normalized to the characteristic admittance of the particular circuit part, extracted from Table I for the case of JPA[-0.36, +0.36]. The shunting capacitance which is encoded in the trace Y_{in}^m determines the shape of the desired admittance Y_{in}^m , controlling the amplifier performance. The red and blue traces are the admittances before and after shunting with the stub with admittance Y_{in}^m , pulling the red trace into the vicinity of the desired green trace. The open/closed circles indicate the start(4 GHz)/stop(8 GHz) frequency. (b) Separate real (conductance) and imaginary (susceptance) components of $Y_{in}^m[\omega_s/(2\pi)]$ for a single embedding circuit used in the three designs.

Eq. (1). We proceed by making a Fourier transformation and subsequent transition into the rotating frame [48] of the pumping field at frequency ω_p , obtaining:

$$\left[i(\tilde{\Omega}_p - \tilde{\omega}_s) + \frac{\kappa[\tilde{\omega}_s]}{2} \right] \hat{a}_s[\tilde{\omega}_s] - \frac{i\omega_0 \delta_{p,max}^2}{16} \hat{a}_i^\dagger[-\tilde{\omega}_s] = \hat{a}_{in}[\tilde{\omega}_s]. \quad (2)$$

We denote with $\tilde{\Omega}_p = \omega_0 - \omega_p - \omega_0 \delta_{p,max}^2/8$ the effective pump frequency detuning and with $\tilde{\omega}_s = \omega_p - \omega_s$ the signal frequency detuning. The intra-oscillator field operators $\hat{a}_{s,i}$ describing the signal and idler modes are related up to a phase factor to $\hat{\delta}_s$. They obey the standard Heisenberg EOM of the nondegenerate JPA [49, 50] through the four-wave mixing Hamiltonian $\hat{H} = \hbar\tilde{\Omega}_p(\hat{a}_s^\dagger \hat{a}_s + \hat{a}_i^\dagger \hat{a}_i) + i\hbar(g/2)(\hat{a}_s^\dagger \hat{a}_i^\dagger - \hat{a}_s \hat{a}_i)$ where $g = 2\Lambda\bar{n}$ is a Kerr-like nonlinearity [8, 50] with $\Lambda\bar{n} \sim \omega_0 \delta_{p,max}^2/16$ being the product of oscillator nonlinearity and the large average number of quanta $\bar{n} \gg 1$ in the oscillator. The solution of the Heisenberg EOM gives the oscillator susceptibility, linking the intra-oscillator field to the input field. The inverse susceptibility matrix χ^{-1} is the coefficient matrix of Eq. (2) and its adjoint equation; $\chi[\tilde{\omega}_s]^{-1} \cdot \hat{\mathbf{a}}[\tilde{\omega}_s] = \hat{\mathbf{a}}_{in}[\tilde{\omega}_s]$ where $\hat{\mathbf{a}}_{in} = (\hat{a}_{in}[\tilde{\omega}_s], \hat{a}_{in}^\dagger[-\tilde{\omega}_s])^T$ and $\hat{\mathbf{a}} = (\hat{a}_s[\tilde{\omega}_s], \hat{a}_i^\dagger[-\tilde{\omega}_s])^T$ [8, 44]. By inverting χ^{-1} and evaluating the element χ_{11} , we determine the photon number gain $G_s[\tilde{\omega}_s] = \mathcal{C}_1 |1 - \text{Re}[\kappa[\tilde{\omega}_s]] \chi_{11}[\tilde{\omega}_s]|^2$ which can be understood as a reflection coefficient at the JJO larger than one and \mathcal{C}_1 is a circuit dependent correction factor. A similar equation holds for the idler field. Knowing the gain, we can estimate the noise added by the nondegenerate JPA by using Ref. [50]. We modify

their result to account for the complete noise referred to the input of the amplifier, consisting of minimum half a photon of shot noise per second and per Hz of bandwidth amplified from the signal and also from the idler field; in total $T_N[\tilde{\omega}_s] = \mathcal{C}_2^{-1}(\hbar\omega_p/k_B - (2\hbar\tilde{\omega}_s/k_B)\{(1/4 + (G[0]/3)(\omega/(1+\omega^2))^2)^{1/2} - (G[0]/3)^{1/2}\omega/(1+\omega^2)\})$. Here, \mathcal{C}_2 is another circuit dependent correction factor and $\omega = \tilde{\omega}_s|\chi_{11}[0]$. For $\tilde{\omega}_s = 0$ this is the fundamental result of the Haus-Caves theorem [4, 51] and for $\tilde{\omega}_s \neq 0$ we obtain an approximate relation of the noise in our amplifier for small detuning.

C. Embedding circuit

We now describe how the two independent JJOs function as one single JPA via their surrounding circuit, c.f. Fig. 1(a). The strong coherent pump tone is applied together with the weak quantum signal to the same input port (1) of a superconducting branch-line coupler. Our amplifier concept contributes a passive and ultra low-loss signal routing functionality to the circuit toolbox that can in cQED applications be combined with existing nonreciprocal circuits to filter out parasitic photons that are generated at the input port (1) of our amplifier. The voltage amplitudes which propagate to ports (2), (3) and (4) are described by a scattering relation, $[\mathbf{S}][\mathbf{V}^\rightarrow] = [\mathbf{V}^\leftarrow]$, where $[\mathbf{V}^\rightarrow, \leftarrow]$ are the ingoing (\rightarrow) and outgoing (\leftarrow) 4-component voltage waves applied to ports (1)-(4) and $[\mathbf{S}] = \frac{1}{\sqrt{2}} \begin{pmatrix} 0 & 1 & i & 0 \\ 1 & 0 & 0 & i \\ i & 0 & 0 & 1 \\ 0 & i & 1 & 0 \end{pmatrix}$ is unitary for a lossless ideal branch-line coupler. An input voltage $V^\rightarrow = V_p[\omega_p] \exp(-i\theta_p) + \hat{V}_{in}[\omega_s] \exp(-i\theta_s)$ applied only to port (1), is divided equally between the ports (2) and (3) together with a *relative* phase shift of $\pi/2$. Port (4) receives no signal in this case. The divided signals leaving ports (2) and (3) couple via the embedding circuits of dimensions $\{l_i, s_i\}$ to the JJOs in which they are amplified and reflected. Ideally, the reflected signals still carry this *relative* phase shift of $\pi/2$ and are back-coupled to ports (2) and (3). An evaluation of the output voltages via the $[\mathbf{S}]$ -matrix shows that now the divided signals combine again constructively at port (4) whereas port (1) receives no signal. We visualize this effect in Fig. 2 and show that the routing of the signals in our circuit is entirely passive and not susceptible to loss within the amplifier bandwidth. For a nondegenerate JPA which preserves the input phase(s) at the output [4], we assume without loss of generality $\theta_p = \theta_s = \pi/2$ at port (1). The density plots for the electric field between the ground plane and the wiring circuit (c.f. Fig. 1(c)), $|\mathbf{E}(\mathbf{r})|$, using this choice of phases show the directional operation on the branch-line coupler. The calculated scattering parameter magnitudes for our circuit are shown in the same figure. They are related to powers ($\propto V^2$) and quantify the signal distribution, yielding an almost perfect realization of the ideal $[\mathbf{S}]$ -matrix over the envisioned operation bandwidth of the JPA.

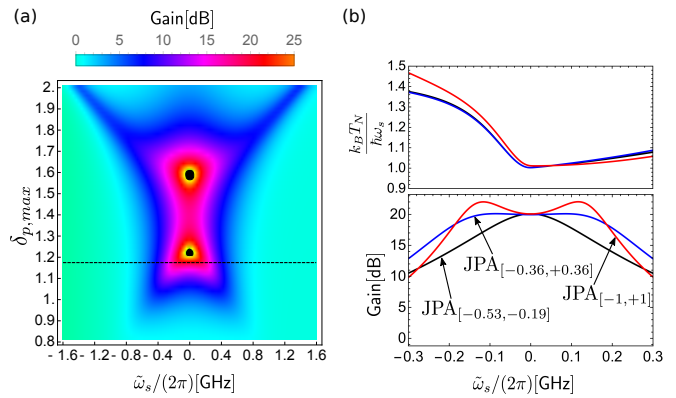


FIG. 4. **Amplifier performance.** (a) Power gain as a function of signal frequency detuning $\tilde{\omega}_s$ and pumping amplitude $\delta_{p,max}$ for JPA[-0.36,+0.36]. The black dashed line indicates the optimal (lowest power) pumping amplitude to achieve a flat gain profile of about 20 dB. Black regions distinguish high-gain regimes $\gg 25$ dB but with significantly decreased bandwidth. (b) Approximate shape of the noise temperature referred to the input and optimal power gain as a function of signal frequency detuning for the three designs.

We design the embedding circuit by visualizing the voltage reflection coefficient and, hence, the normalized complex transmission line input admittance $Y_{in}/Y_c = (Y_L + iY_c \tanh(\gamma l)) / (Y_c + iY_L \tanh(\gamma l))$ in the polar plane of the Smith chart [46, 52], c.f. Fig 3(a) and Fig. 1(a). Here, Y_c is the characteristic admittance of the particular microstrip segment, Y_L is the termination admittance, γ is the complex propagation constant [48, 53] and l is the length. Finally, the complex valued admittance is plotted in the Smith chart. A point represents the intersection between the corresponding conductance circle, where the normalized conductance is indicated on the horizontal axis and the susceptance circle, where the normalized susceptance is indicated around the Smith chart. For a given admittance, a change in l will rotate the trace in the Smith chart by $2\gamma l$ and connecting admittances of different values will lead to jumps in the overall admittance (compare with the traces in Fig. 3(a)), transforming the admittance and changing the shape of the conductance and the slope of the susceptance of Y_{in}'''' like shown in Fig. 3(b). The correction factors for gain and noise are given by the scattering parameters and the coupling to the JJOs, $\mathcal{C}_1 = |S_{41}[\tilde{\omega}_s]|$ shown in Fig. 2(d) and $\mathcal{C}_2 = (|S_{21}[\tilde{\omega}_s]| + |S_{31}[\tilde{\omega}_s]|) \times \mathcal{T}$ where the scattering parameters are the ones shown in Fig. 2(c) and \mathcal{T} is the signal coupling to the JJOs, being a factor between '1' and '0.95', c.f. [48].

The directional signal routing in our device relies fundamentally on the imposed relative phase difference of $\pi/2$ between the two JJOs and we have to estimate the influence of slightly detuned JJOs. We find that a relative plasma frequency detuning of 200 MHz will cause an additional phase difference of $\sim \pi/18$ in the outgoing amplified signals. While this will only slightly change the

coupler directivity S_{41} in Fig. 2(d), the return loss S_{11} of the device port (1) indicated in the same figure will degrade to -12 dB from its original value of < -25 dB [48]. In the aforementioned situation, the two JJOs differ also in their gain by about 0.8 dB which has a negligible influence.

III. RESULTS

Figure 4 and Table I summarize our results for gain, noise and the designs of the JPA. While we obtain the best performance for JPA[-0.36,+0.36], the other two designs show the influence of the real and imaginary part of Y_{in}'''' on the amplifier performance. For design JPA[-0.36,+0.36], the term $-\tilde{\omega}_s + \text{Im}[\kappa[\tilde{\omega}_s]]$ in Eq. (2) assumes the smallest frequency dependence with a slope symmetric around zero, maximizing the amplification bandwidth. For the other two designs the same term contains a much stronger frequency dependence and the slope is not symmetric around zero, resulting in a decreased performance, therefore, bandwidth of the amplifier. The dynamic range for a single Josephson junction oscillator operated close to the bifurcation point scales with $P_{dyn} \propto I_c^2/Q$ [39], where $Q \approx \omega_0 \text{Re}[Z_{in}'''] C_0$. The two JJOs in our circuit effectively double the critical current which increases the dynamic range by a factor of four.

It can be further increased by increasing the current density of the Josephson junctions which is rather limited for Al/AlOx/Al junctions. Higher values of up to $J_c = 78$ kA/cm² are reachable with AlN barriers in Nb-based circuits [54] which would increase the dynamic range by up to three orders of magnitude compared to existing JPAs and would enable to read-out large arrays of detectors containing some thousands of pixels [5] or multiple qubits [11]. In this amplifier technology, however, the SQUID cannot be fabricated anymore using the well established angle-evaporation technique and one has to rely on trilayer Josephson junctions [40, 41].

IV. DISCUSSION

We have designed and analyzed a broadband and compact JPA with integrated directionality which adds only about one single photon of total noise at the input. While our proposed device is fully reciprocal, nonreciprocity can be achieved by combining our device with existing nonreciprocal devices at the input of our amplifier. Employing existing high-current density Josephson junctions would increase the dynamic range significantly compared to existing JPAs. Our embedding circuit is general enough to tune the gain of signal and idler modes independently, providing interesting opportunities to tailor nonclassical microwave light [55, 56].

In closing, we address two specific examples, where our proposed amplifier adds improved functionality.

In cQED, an increasing number of experiments reads out a cavity state by using a one-port JPA together with a nonreciprocal device, which directs the amplified field to the post-processing electronics and protects the cavity from noise. Commercially available nonreciprocal magnetic circulators are mainly characterized by their isolation, which quantifies to what extent the circulator can block radiation emitted towards the quantum sensitive cavity. A typical isolation value for these commercial circulators amounts to -20 dB. This is also true for the novel non-magnetic circulator reported in [25]. As a consequence, the amplified vacuum noise of such a one-port JPA, emitted towards the nonreciprocal device, results in one parasitic photon per second and per Hz of bandwidth, transmitted towards the cavity. A desired cavity field, amplified by the JPA, will further enhance the number of these parasitic photons. Improvement over a broad bandwidth is difficult to achieve.

Our amplifier concept, provides an attractive solution since it emits only amplified vacuum noise from input port (1) and emits separately the amplified field and vacuum noise from output port (4). Therefore, a nonreciprocal device with a given isolation connected to input port (1), reduces also the parasitic photons transmitted through the nonreciprocal device towards the cavity.

In another example, in astronomical instrumentation [57, 58] microresonator arrays of 20.000 pixels have been realized recently. The dissipation and the noise of the read-out amplifiers is becoming a very important limiting factor. In addition, in order to reduce standing waves in the read-out signal it would be beneficial to integrate an amplifier on the same chip with the MKID array. The fabrication of our amplifier is compatible with the currently used MKID technology. Our amplifier concept makes it possible to connect the read-out line of the MKID array directly to input port (1). The combination of low noise, broad-band and integrability make our proposed amplifier very suitable for use with MKID arrays.

ACKNOWLEDGMENTS

We acknowledge funding through the European Research Council Advanced Grant No. 339306 (METIQUIM). We have had fruitful discussions with Karl Jacobs and Patrick Pütz of KOSMA, 1. Physikalisches Institut, Universität zu Köln, Germany, related to the micro-fabrication of the circuit and the various Josephson junction technologies. Furthermore, we appreciated helpful comments from Udson Mendes, Université de Sherbrooke, Canada, on the general content. We would like to thank the referees for critical and essential comments on the input noise created by our parametric amplifier and for other general comments which helped to improve the manuscript.

-
- [1] B. D. Josephson, “Coupled superconductors,” *Rev. Mod. Phys.* **36**, 216 (1964).
- [2] B. Yurke, P. G. Kaminsky, R. E. Miller, E. A. Whittaker, A. D. Smith, A. H. Silver, and R. W. Simon, “Observation of 4.2-K equilibrium-noise squeezing via a Josephson-parametric amplifier,” *Phys. Rev. Lett.* **60**, 764 (1988).
- [3] B. Yurke, L. R. Corruccini, P. G. Kaminsky, L. W. Rupp, A. D. Smith, A. H. Silver, R. W. Simon, and E. A. Whittaker, “Observation of parametric amplification and deamplification in a Josephson parametric amplifier,” *Phys. Rev. A* **39**, 2519 (1989).
- [4] C. M. Caves, “Quantum limits on noise in linear amplifiers,” *Phys. Rev. D* **26**, 1817 (1982).
- [5] P. K. Day, H. G. LeDuc, B. A. Mazin, A. Vayonakis, and J. Zmuidzinas, “A broadband superconducting detector suitable for use in large arrays,” *Nature* **425**, 817 (2003).
- [6] J. Zmuidzinas, “Superconducting microresonators: Physics and applications,” *Annu. Rev. Condens. Matter Phys.* **3**, 169 (2012).
- [7] M. H. Devoret and R. J. Schoelkopf, “Superconducting circuits for quantum information: An outlook,” *Science* **339**, 1169 (2013).
- [8] A. A. Clerk, M. H. Devoret, S. M. Girvin, F. Marquardt, and R. J. Schoelkopf, “Introduction to quantum noise, measurement and amplification,” *Rev. Mod. Phys.* **82**, 1155 (2010).
- [9] A. Bienfait, J. J. Pla, Y. Kubo, M. Stern, X. Zhou, C. C. Lo, C. D. Weis, T. Schenkel, M. L. W. Thewalt, D. Vion, D. Esteve, B. Julsgaard, K. Molmer, J. J. L. Morton, and P. Bertet, “Reaching the quantum limit of sensitivity in electron spin resonance,” *Nat. Nanotech.* **11**, 253 (2015).
- [10] A. Bienfait, J. J. Pla, Y. Kubo, X. Zhou, M. Stern, C. C. Lo, C. D. Weis, T. Schenkel, D. Vion, D. Esteve, J. J. L. Morton, and P. Bertet, “Controlling spin relaxation with a cavity,” *Nature* **531**, 74 (2016).
- [11] R. Barends, J. Kelly, A. Megrant, A. Veitia, D. Sank, E. Jeffrey, T. C. White, J. Mutus, A. G. Fowler, B. Campbell, Y. Chen, Z. Chen, B. Chiaro, A. Dunsworth, C. Neill, P. O’Malley, P. Roushan, A. Vainsencher, J. Wenner, A. N. Korotkov, A. N. Cleland, and John M. Martinis, “Superconducting quantum circuits at the surface code threshold for fault tolerance,” *Nature* **508**, 500 (2014).
- [12] M. Hofheinz, H. Wang, M. Ansmann, R. C. Bialczak, E. Lucero, M. Neeley, A. D. O’Connell, D. Sank, J. Wenner, J. M. Martinis, and A. N. Cleland, “Synthesizing arbitrary quantum states in a superconducting resonator,” *Nature* **459**, 546 (2009).
- [13] M. Hofheinz, E. M. Weig, M. Ansmann, R. C. Bialczak, E. Lucero, M. Neeley, A. D. O’Connell, H. Wang, J. M. Martinis, and A. N. Cleland, “Generation of Fock states in a superconducting quantum circuit,” *Nature* **454**, 310 (2008).
- [14] F. Mallet, F. R. Ong, A. Palacios-Laloy, F. Nguyen, P. Bertet, D. Vion, and D. Esteve, “Single-shot qubit readout in circuit quantum electrodynamics,” *Nat. Phys.* **5**, 791 (2009).
- [15] S. Barzanjeh, M. Wulf, M. Peruzzo, M. Kalraee, P. B. Dieterle, O. Painter, and J. M. Fink, “Mechanical on-chip microwave circulator,” *Nature Commun.* **8**, 953 (2017).
- [16] N. R. Bernier, L. D. Tóth, A. Koottandavida, M. Ioannou, D. Malz, A. Nunnenkamp, A. K. Feofanov, and T. J. Kippenberg, “Nonreciprocal reconfigurable microwave optomechanical circuit,” *Nature Commun.* **8**, 604 (2017).
- [17] G. A. Peterson, F. Lecocq, K. Cicak, R. W. Simmonds, J. Aumentado, and J. D. Teufel, “Demonstration of efficient nonreciprocity in a microwave optomechanical circuit,” *Phys. Rev. X* **7**, 031001 (2017).
- [18] K. Fang, J. Luo, A. Metelmann, M. H. Matheny, F. Marquardt, A. A. Clerk, and O. Painter, “Generalized nonreciprocity in an optomechanical circuit via synthetic magnetism and reservoir engineering,” *Nat. Phys.* **13**, 465 (2017).
- [19] F. Ruesink, M. Miri, A. Alú, and E. Verhagen, “Nonreciprocity and magnetic-free isolation based on optomechanical interactions,” *Nat. Commun.* **7**, 13662 (2016).
- [20] Z. Shen, Y.-L. Zhang, Y. Chen, C.-L. Zou, Y.-F. Xiao, X.-B. Zou, F.-W. Sun, G.-C. Guo, and C.-H. Dong, “Experimental realization of optomechanically induced nonreciprocity,” *Nat. Photonics* **10**, 657 (2016).
- [21] X.-W. Xu, Y. Li, A.-X. Chen, and Y.-X. Liu, “Nonreciprocal conversion between microwave and optical photons in electro-optomechanical systems,” *Phys. Rev. A* **93**, 023827 (2016).
- [22] M. Hafezi and P. Rabl, “Optomechanically induced nonreciprocity in microring resonators,” *Opt. Express* **20**, 7672 (2012).
- [23] A. Kamal, J. Clarke, and M. H. Devoret, “Noiseless nonreciprocity in a parametric active device,” *Nat. Phys.* **7**, 311 (2011).
- [24] J. Kerckhoff, K. Lalumière, B. J. Chapman, A. Blais, and K. W. Lehnert, “On-chip superconducting microwave circulator from synthetic rotation,” *Phys. Rev. Appl.* **4**, 034002 (2015).
- [25] Benjamin J. Chapman, Eric I. Rosenthal, Joseph Kerckhoff, Bradley A. Moores, Leila R. Vale, J. A. B. Mates, Gene C. Hilton, Kevin Lalumière, Alexandre Blais, and K. W. Lehnert, “Widely tunable on-chip microwave circulator for superconducting quantum circuits,” *Phys. Rev. X* **7**, 041043 (2017).
- [26] J. Koch, A. A. Houck, K. Le Hur, and S. M. Girvin, “Time-reversal-symmetry breaking in circuit-QED-based photon lattices,” *Phys. Rev. A* **82**, 043811 (2010).
- [27] A. Metelmann and A. A. Clerk, “Nonreciprocal photon transmission and amplification via reservoir engineering,” *Phys. Rev. X* **5**, 021025 (2015).
- [28] L. Ranzani and J. Aumentado, “Graph-based analysis of nonreciprocity in coupled-mode systems,” *New J. Phys.* **17**, 023024 (2015).
- [29] A. Kamal, A. Roy, J. Clarke, and M. H. Devoret, “Asymmetric frequency conversion in nonlinear systems driven by a biharmonic pump,” *Phys. Rev. Lett.* **113**, 247003 (2014).
- [30] N. A. Estep, D. L. Sounas, J. Soric, and A. Alú, “Magnetic-free non-reciprocity and isolation based on parametrically modulated coupled-resonator loops,” *Nat. Phys.* **10**, 923 (2014).
- [31] K. M. Sliwa, M. Hatridge, A. Narla, S. Shankar, L. Frunzio, R. J. Schoelkopf, and M. H. Devoret, “Reconfigurable Josephson circulator/directional amplifier,”

- Phys. Rev. X **5**, 041020 (2015).
- [32] B. Abdo, K. Sliwa, S. Shankar, M. Hatridge, L. Frunzio, R. Schoelkopf, and M. Devoret, “Josephson directional amplifier for quantum measurement of superconducting circuits,” Phys. Rev. Lett. **112**, 167701 (2014).
- [33] B. Abdo, K. Sliwa, L. Frunzio, and M. Devoret, “Directional amplification with a Josephson circuit,” Phys. Rev. X **3**, 031001 (2013).
- [34] F. Lecocq, L. Ranzani, G. A. Peterson, K. Cicak, R. W. Simmonds, J. D. Teufel, and J. Aumentado, “Nonreciprocal microwave signal processing with a field-programmable josephson amplifier,” Phys. Rev. Applied **7**, 024028 (2017).
- [35] C. Macklin, K. O’Brien, D. Hover, M. E. Schwartz, V. Bolkhovskiy, X. Zhang, W. D. Oliver, and I. Siddiqi, “A near-quantum-limited josephson traveling-wave parametric amplifier,” Science **350**, 307 (2015).
- [36] R. Vijay, M. H. Devoret, and I. Siddiqi, “Invited review article: The Josephson bifurcation amplifier,” Rev. Sci. Instrum. **80**, 111101 (2009).
- [37] I. Siddiqi, R. Vijay, F. Pierre, C. M. Wilson, M. Metcalfe, C. Rigetti, L. Frunzio, and M. H. Devoret, “RF-driven Josephson bifurcation amplifier for quantum measurement,” Phys. Rev. Lett. **93**, 207002 (2004).
- [38] I. Siddiqi, R. Vijay, F. Pierre, C. M. Wilson, L. Frunzio, M. Metcalfe, C. Rigetti, R. J. Schoelkopf, M. H. Devoret, D. Vion, and D. Esteve, “Direct observation of dynamical bifurcation between two driven oscillation states of a Josephson junction,” Phys. Rev. Lett. **94**, 027005 (2005).
- [39] V. E. Manucharyan, E. Boaknin, M. Metcalfe, R. Vijay, I. Siddiqi, and M. Devoret, “Microwave bifurcation of a Josephson junction: Embedding-circuit requirements,” Phys. Rev. B **76**, 014524 (2007).
- [40] M. P. Westig, K. Jacobs, J. Stutzki, M. Schultz, M. Justen, and C. E. Honingh, “Balanced superconductor-insulator-superconductor mixer on a 9 μm silicon membrane,” Supercond. Sci. Technol. **24**, 085012 (2011).
- [41] M. P. Westig, M. Justen, K. Jacobs, J. Stutzki, M. Schultz, F. Schomacker, and C. E. Honingh, “A 490 GHz planar circuit balanced Nb-Al₂O₃-Nb quasiparticle mixer for radio astronomy: Application to quantitative local oscillator noise determination,” J. Appl. Phys. **112**, 093919 (2012).
- [42] We study the functionality of the circuit by simulations in CST [59] and find consistence with an analytical model describing our microstrip geometry up to an uncertainty of 3% [48, 53], assuming a normal-state resistance of $\rho_n = 0.1 \mu\Omega\text{cm}$ and a superconducting gap of $\Delta = 0.18 \text{ meV}$.
- [43] J. Y. Mutus, T. C. White, R. Barends, Yu Chen, Z. Chen, B. Chiaro, A. Dunsworth, E. Jeffrey, J. Kelly, A. Megrant, C. Neill, P. J. J. O’Malley, P. Roushan, D. Sank, A. Vainsencher, J. Wenner, K. M. Sundqvist, A. N. Cleland, and J. M. Martinis, “Strong environmental coupling in a Josephson parametric amplifier,” Appl. Phys. Lett. **104**, 263513 (2014).
- [44] T. Roy, S. Kundu, M. Chand, A. M. Vadiraj, A. Ranadive, N. Nehra, M. P. Patankar, J. Aumentado, A. A. Clerk, and R. Vijay, “Broadband parametric amplification with impedance engineering: Beyond the gain-bandwidth product,” Appl. Phys. Lett. **107**, 262601 (2015).
- [45] R. Sorrentino and L. Roselli, “A new simple and accurate formula for microstrip radial stub,” IEEE Microw. Guided Wave Lett. **2**, 480 (1992).
- [46] R. E. Collin, *Foundations for Microwave Engineering* (Wiley-IEEE Press, 1992).
- [47] M. Tinkham, *Introduction to Superconductivity*, 2nd ed. (Dover Publications, Inc., 2004).
- [48] See Supplemental Material at [URL will be inserted by publisher] for additional details.
- [49] C. W. Gardiner and M. J. Collett, “Input and output in damped quantum systems: Quantum stochastic differential equations and the master equation,” Phys. Rev. A **31**, 3761 (1985).
- [50] C. Laflamme and A. A. Clerk, “Quantum-limited amplification with a nonlinear cavity detector,” Phys. Rev. A **83**, 033803 (2011).
- [51] H. A. Haus and J. A. Mullen, “Quantum noise in linear amplifiers,” Phys. Rev. **128**, 2407 (1962).
- [52] P. H. Smith, “Transmission line calculator,” Electronics **12**, 29 (1939).
- [53] R. L. Kautz, “Picosecond pulses on superconducting striplines,” J. Appl. Phys. **49**, 308 (1978).
- [54] T. Zijlstra, C. F. J. Lodewijk, N. Vercruyssen, F. D. Tichelaar, D. N. Loudkov, and T. M. Klapwijk, “Epitaxial aluminum nitride tunnel barriers grown by nitridation with a plasma source,” Appl. Phys. Lett. **91**, 233102 (2007).
- [55] A. D. Armour, B. Kubala, and J. Ankerhold, “Josephson photonics with a two-mode superconducting circuit,” Phys. Rev. B **91**, 184508 (2015).
- [56] M. Westig, B. Kubala, O. Parlavecchio, Y. Mukharsky, C. Altimiras, P. Joyez, D. Vion, P. Roche, M. Hofheinz, D. Esteve, M. Trif, P. Simon, J. Ankerhold, and F. Portier, “Emission of non-classical radiation by inelastic cooper pair tunneling,” Phys. Rev. Lett. **119**, 137001 (2017).
- [57] J. J. A. Baselmans, J. Bueno, S. J. C. Yates, O. Yurduseven, N. Llombart, K. Karatsu, A. M. Baryshev, L. Ferrari, A. Endo, D. J. Thoen, P. J. de Visser, R. M. J. Janssen, V. Murugesan, E. F. C. Driessen, G. Coiffard, J. Martin-Pintado, P. Hargrave, and M. Griffin, “A kilopixel imaging system for future space based far-infrared observatories using microwave kinetic inductance detectors,” Astron. Astrophys. **601**, A89 (2017).
- [58] Lorenza Ferrari, Ozan Yurduseven, Nuria Llombart, Stephen J. C. Yates, Juan Bueno, Vignesh Murugesan, David J. Thoen, Akira Endo, Andrey M. Baryshev, and Jochem J. A. Baselmans, “Antenna coupled mkid performance verification at 850 ghz for large format astrophysics arrays,” IEEE Trans. THz Sci. Technol. **8**, 127 (2018).
- [59] CST - Computer Simulation Technology, URL = <https://www.cst.com>.

Josephson parametric reflection amplifier with integrated directionality: Supplemental material

M. P. Westig (m.p.westig@tudelft.nl) and T. M. Klapwijk (t.m.klapwijk@tudelft.nl)

Kavli Institute of NanoScience, Delft University of Technology, Lorentzweg 1, 2628 CJ Delft, The Netherlands

In this supplemental information we provide additions to several aspects of the main text which in our believe are worth-while discussing in more detail. We solve the equation of motion for the single nonlinear Josephson junction oscillators (JJO), both when a strong pump tone and a weak quantum signal is applied to their input. This yields the gain and noise for the single JJOs when operated as a Josephson parametric amplifier (JPA). Additionally, we provide a suitable input-output formalism for the JPA microwave fields in order to quantify the parametric gain and noise of the device when two JJOs are combined to form a single directional JPA, being the topic of the main text. Also, we add useful material summarizing a design and its characterization of a dielectric loaded coplanar waveguide-to-microstrip transformer circuit. This circuit provides the possibility to connect our microstrip JPA to other quantum circuits or to the microwave cabling of the experiment, often designed in coplanar waveguide technology. Finally, we provide an analytical model for the dispersion relation on the superconducting microstrip transmission line which allows to evaluate the design changes of the JPA circuit as a function of the aluminum normal-state resistivity (treated in this work) or as a function of the resistivity of any other superconducting material which is chosen to pattern the circuit.

EQUATION OF MOTION FOR THE SINGLE JJO ACTING AS NONDEGENERATE JPA

The tone which is pumping the two JJOs through ports (2) and (3), shown in Fig. 1(a) of the main text, can be described as a pumping current source connected in parallel to the input admittance $Y_{in}^{''''}[\tilde{\omega}_s]$ of the JJO's electromagnetic (EM) environment (acting as the source admittance of the pumping current source) and to the respective JJO; the JJO is attached in a SQUID configuration and acts effectively as a magnetic-flux tunable nonlinear oscillator.

For reasons of simplicity, we will consider in the following treatment only a single JJO which acts as a single nondegenerate JPA. The microwave routing in our circuit which finally combines the two separate nondegenerate JPAs is explained in the main text.

The JJO is characterized by the nonlinear Josephson inductance $L_J(\Phi) = h/(4\pi e I_c(\Phi))$ and by the shunting capacitor C_0 (compare with Fig. 1(a) of the main text). One can further specify the JJO through its characteristic admittance $Y_0 = \sqrt{C_0/L_J(\Phi)}$, fundamental reso-

nance frequency $\omega_0 = 1/\sqrt{L_J(\Phi)C_0}$ and quality factor $Q \approx \omega_0 \text{Re}[Z_{in}^{''''}] C_0$. Here, it is as usual $Y_{in}^{''''} = (Z_{in}^{''''})^{-1}$. $L_J(\Phi)$ is tunable through the external magnetic flux Φ piercing through the SQUID loop. Since C_0 is much larger than the intrinsic capacitance of the Josephson junctions, C_J , we neglect the latter capacitance in the following. Note that here $I_c(\Phi) = 2i_c \left| \cos\left(\frac{\pi\Phi}{\phi_0}\right) \right|$ is the total critical current of the Josephson junctions in the SQUID, i_c denotes the critical current of each of the two Josephson junctions in the SQUID and $\phi_0 = h/(2e)$ is the flux quantum (not to be confused with the symbol for the node flux of a transmission line we will introduce later). Therefore, we assume that the two junctions are identical. The case of non-identical junctions is easily incorporated by considering a SQUID asymmetry due to which one cannot adjust anymore a perfectly zero critical current. We also assume a negligible inductance of the SQUID loop arms which has to be compared to the total Josephson inductance. On the other hand, for small loop inductance L_{loop} , but still sizable against $L(\Phi)$, the minimal reachable critical current in the SQUID increases as $\pi L_{loop} I_c / \phi_0$ but is in most of the practical cases still small enough to reach a large enough Josephson inductance or equivalently to reach a small enough plasma frequency ω_0 .

Like in the main text, $\tilde{\omega}_s = \omega_p - \omega_s$ denotes the detuning of the signal from the pump frequency and $\tilde{\omega}_p = \omega_0 - \omega_p$ is the detuning of the pump frequency from the plasma frequency ω_0 of the JJO. For not too large detuning $\tilde{\omega}_s$ and $\tilde{\omega}_p$ from the center (design) frequency of the EM environment of 6 GHz, $Y_{in}^{''''} \approx (30.0 \Omega)^{-1}$ is to good approximation real valued. Furthermore, $Y_0 \approx (5.45 \Omega)^{-1}$ for the parameter regime envisioned in this work for a tunable JJO frequency of $\omega_0 = 1/\sqrt{L_J(\Phi)C_0} \approx 2\pi \cdot 7.3$ GHz, where $C_0 = 4.0$ pF is fixed through its parallel plate geometry in the microstrip circuitry and $L_J = 0.12$ nH in this case but still magnetic-flux tunable as said before. With this (arbitrary) choice of ω_0 we anticipate the yet to be derived result (compare with Eq. (S23)) that the plasma frequency shifts with increasing pumping amplitude.

For the purpose of our paper, the dynamics of the phase difference $\delta \propto 2\pi\Phi/\phi_0 \pmod{2\pi}$ of the JJO is well described by the resistively and capacitively shunted Josephson junction (RCSJ) model [M. Tinkham, *Introduction to Superconductivity*, Dover Publications, Inc., 2nd edition, 2004]. The solution of the RCSJ model yields the intra-oscillator field both for the strong pump tone and for the noise (or the weak signal) which are leak-

ing via the transmission line into the JJO (cf. Fig. S2). We want to separate δ into two parts. A classical part, δ_p , belonging to the strong pump and a quantum part, δ_s , belonging to the noise on the transmission line or/and to a weak signal which is amplified by the device.

Although the RCSJ model is originally formulated for a single Josephson junction with only one critical current i_c , it can be readily translated to apply to a Josephson junction SQUID consisting of two junctions in which the critical current is magnetic-flux tunable as described before. We, therefore, substitute $I_c(\Phi)$ in the RCSJ model and treat it as the (total) critical current of the system, yet adjustable. Hence, the superconducting response of the Josephson junction SQUID is covered by a term $I_c(\Phi) \sin(\delta(t))$ with the phase difference δ defined before and I_c being now a magnetic-flux tunable supercurrent. Furthermore, since we want to operate the JJO in the zero-voltage state, we assume that it is only shunted by the radio-frequency (*rf*) resistance of its EM environment and not by its normal-state resistance which would otherwise appear in the voltage-carrying state of the junction. In this particular situation, the RCSJ model goes over into the Duffing equation after Taylor expansion of the ' $\sin(\delta(t))$ ' term in the RCSJ model and keeping only the first non-linear term. The Duffing equation finally reads:

$$\frac{C_0\phi_0}{2\pi}\ddot{\delta}(t) + \frac{Y_{in}''''\phi_0}{2\pi}\dot{\delta}(t) + I_c(\Phi) \left[\delta(t) - \frac{1}{6}\delta(t)^3 \right] = I(t) , \quad (S1)$$

where C_0 is the shunting capacitance of the JJO and Y_{in}'''' is the input admittance of the EM environment at the pumping frequency. Furthermore, $I(t) = I_p(t) + \hat{I}_s(t)$ is the total microwave pump current applied externally to the JJO, consisting of the strong pump current I_p which is treated in the following as a classical signal. Additionally, the JJO is also pumped by the quantum component \hat{I}_s via the same port like the pump current.

Dividing Eq. (S1) by the term ' $C_0\phi_0/(2\pi)$ ', the Duffing equation assumes a form in which the characteristic

parameters of the JJO explicitly appear:

$$\ddot{\delta}(t) + \frac{Y_{in}''''}{C_0}\dot{\delta}(t) + \omega_0^2 \left[\delta(t) - \frac{1}{6}\delta(t)^3 \right] = \omega_0^2 \frac{I(t)}{I_c(\Phi)} , \quad (S2)$$

where we identify the plasma frequency of the JJO as $\omega_0 = \sqrt{\frac{2\pi I_c(\Phi)}{\phi_0 C_0}}$ or equivalently written as $\omega_0 = 1/\sqrt{L_J(\Phi)C_0}$ as stated already before.

In order to prepare the evaluation of the intra-oscillator field δ of the pumped JJO we proceed in two steps. First, we are interested in the large-signal solution of Eq. (S2), very similar to the solution strategy in quantum SIS heterodyne mixer theory [J. R. Tucker and M. J. Feldman, Rev. Mod. Phys. **57**, 1055, 1985] when predicting the current-voltage characteristic, gain and noise of the mixer device. In a second step described further below, we rewrite Eq. (S2) to account for a weak quantum signal which is coupled to the oscillator; this form of the equation is used to calculate the parametric gain and noise of the JPA in the main text of our work.

For the first step, we assume that no quantum signal is coupled into the oscillator, $\hat{I}_s(t) = 0$, and only the strong pump current $I_p(t) = \bar{I}_p \cos(\omega_p t)$ is applied pumping the nonlinear JJO. In this situation the system behaves like a classical nonlinear oscillator and we do not have to further specify the complications which have to be introduced when describing the system quantum mechanically (like we will do further below after the following brief preparation).

In the method of harmonic balance one assumes a solution of the Duffing equation (S2) of the form $\delta_p = a \cos(\omega_p t) + b \sin(\omega_p t)$ or equivalently $\delta_p = \delta_{p,max} \cos(\omega_p t - \varphi)$ where $\delta_{p,max}^2 = a^2 + b^2$ and $\tan(\varphi) = b/a$. Therefore, we separate the solution into an in-phase ($\propto \cos(\cdot)$) and a quadrature phase ($\propto \sin(\cdot)$) term (I&Q term). After substituting δ_p into (S2) and combining/simplifying the resulting terms one arrives at the following equation system:

$$\begin{aligned} & \cos(\omega_p t) \left[-a\omega_p^2 + \frac{b\omega_p Y_{in}''''}{C_0} + a\omega_0^2 - \frac{1}{6}\omega_0^2 \left(\frac{3a^3}{4} + \frac{3ab^2}{4} \right) - \omega_0^2 \frac{\bar{I}_p}{I_c} \right] \\ & + \sin(\omega_p t) \left[-b\omega_p^2 - \frac{a\omega_p Y_{in}''''}{C_0} + b\omega_0^2 - \frac{1}{6}\omega_0^2 \left(\frac{3b^3}{4} + \frac{3a^2b}{4} \right) \right] \\ & + \cos(3\omega_p t) \left[-\frac{1}{6}\omega_0^2 \left(\frac{a^3}{4} - \frac{3ab^2}{4} \right) \right] \\ & + \sin(3\omega_p t) \left[-\frac{1}{6}\omega_0^2 \left(-\frac{b^3}{4} + \frac{3a^2b}{4} \right) \right] = 0 . \end{aligned} \quad (S3)$$

In the following we will neglect the higher order harmonics $\propto \cos(3\omega_p t)$ and $\propto \sin(3\omega_p t)$. Furthermore, the $\cos(\cdot)$ and $\sin(\cdot)$ terms can be seen as an orthogonal function basis so that we can proceed as follows. Squaring the

first and second line in Eq. (S3) and adding the results leads to the large signal solution of the Duffing equation which after further simplifications assumes the following form:

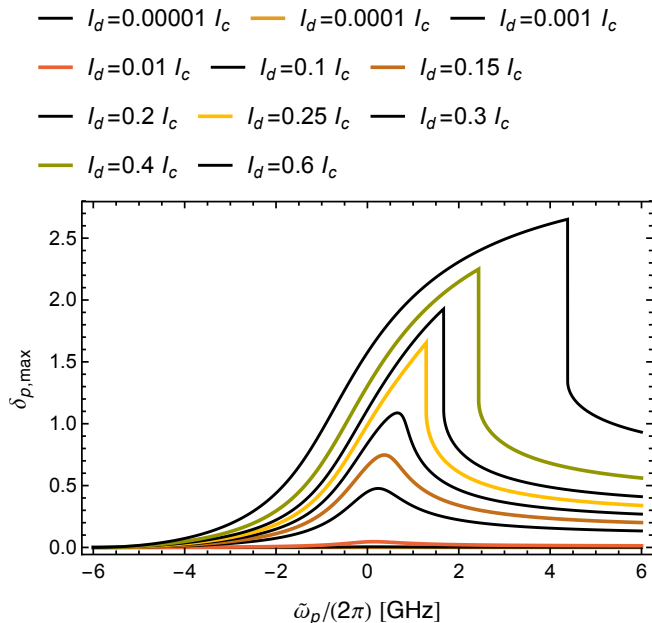


FIG. S1. Nonlinear frequency response of the classically pumped JJO in the large signal picture, evaluated by solving Eq. (S4) for $\delta_{p,max}$. The rms pumping amplitude is expressed in terms of the critical current I_c of the Josephson junction SQUID. Parameters used for the plot: $C_0 = 4$ pF and $(Y_{in}''''[\omega_p])^{-1} = 30 \Omega$ for a constant pump frequency of $\omega_p/(2\pi) = 6$ GHz. The x-axis shows the pump frequency detuning from the plasma frequency $\tilde{\omega}_p/(2\pi) = (1/2\pi)(\omega_0 - \omega_p)$ and the y-axis shows the internal field in the oscillator building up due to the pumping. With increasing pumping amplitude, the maximum response shifts to increasingly positive pump frequency detuning. The optimal operating point of the amplifier is where a small signal change induces a big change in the oscillator dynamics at a detuning of approximately $\tilde{\omega}_p/(2\pi) = 1.5$ GHz or in other words at plasma frequencies of about $\omega_0 = 7.3$ - 7.5 GHz like found consistently in the main text.

$$\left[\left(\omega_p^2 - \omega_0^2 + \frac{\omega_0^2 \delta_{p,max}^2}{8} \right)^2 + \left(\frac{\omega_p Y_{in}''''}{C_0} \right)^2 \right] \delta_{p,max}^2 = \omega_0^4 \frac{\bar{I}_p^2}{I_c^2(\Phi)}. \quad (\text{S4})$$

Equation (S4) describes the full nonlinear frequency response of the JJO in the large-signal picture which we show for different pumping strengths in Fig. S1. For increasing pumping strength, the maximum oscillator frequency response shifts to increasingly large pump frequency detuning and becomes nonlinear as expected from Eq. (S4). This has to be taken into consideration when adjusting the operation frequency of the JPA via the magnetic-flux, tuning ω_0 .

In the second step we aim at understanding the nonlinear oscillator dynamics and, hence, how the parametric amplification is established when we couple along with the strong pump tone, a weak signal or (quantum) noise

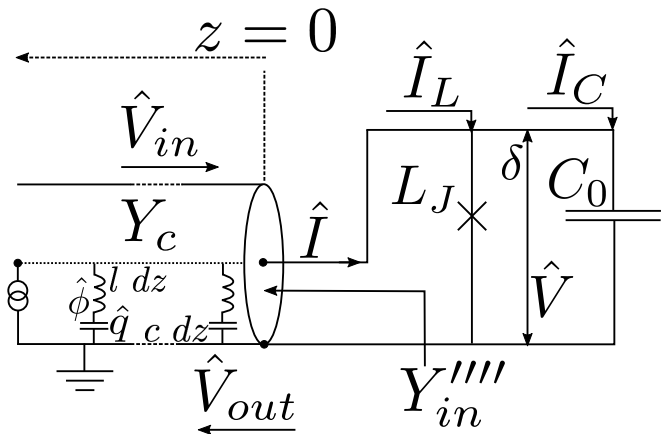


FIG. S2. **Input, output and intra-oscillator (δ) fields in the nonlinear JJO.** The nonlinear oscillator is pumped by a microwave current source and consists of a nonlinear inductor (Josephson junction or SQUID; \times symbol) and linear capacitor connected in parallel to a transmission line of characteristic admittance Y_c , providing the input admittance Y_{in}'''' (compare with Fig. 1(a) of the main text) to the nonlinear oscillator at $z = 0$. This admittance is the only source of dissipation in the system which allows for exchange of energy into and out of the nonlinear oscillator with rate κ . The strong pump and the weak (quantum) noise and signal field leak into the nonlinear oscillator and subsequently the internal oscillator field leaks out again into the transmission line where it is connected to the measurement apparatus. The nonlinear inductance does provide parametric amplification of the weak input field when it is additionally pumped by the strong pumping field. The conjugated quantum variables of the nonlinear oscillator are the phase and charge across the nonlinear inductor and linear capacitor.

into the oscillator. With quantum noise we specifically mean the vacuum fluctuations on the transmission line which are injected into the JPA. We will specify in the next section of this supplemental information what we exactly mean with that and why it is important to discuss this topic when dealing with (quantum) amplification with a phase-preserving, i.e. nondegenerate JPA.

Our following task will be to derive how Eq. (S2) is modified when we couple a weak quantum signal to the nonlinear oscillator; a sketch of this situation is shown in Fig. S2.

To do so, first, we have to describe our circuit quantum mechanically. We will then come back to the derivation of the nonlinear oscillator equation describing pumping through a weak quantum signal further below.

We recall that to perform the circuit quantization, one describes a (quantum) transmission line or an oscillator as a set of noninteracting bosonic modes like shown on the positive z -side in Fig. S2, suggesting an infinite chain of inductors and shunting capacitors in the inside of the transmission line leading to an admittance Y_c [A. O. Caldeira and A. J. Leggett, Ann. Phys. (N. Y.) **149**, 374, (1983)]. This description is well established and is based on the La-

grangian/Hamiltonian formulation of the transmission line and nonlinear oscillator to which the transmission line is connected to (see for an instructive review [A. A. Clerk et al., Rev. Mod. Phys. **82**, 1155, (2010)] and by considering in particular also [M. Devoret, *Quantum Fluctuations in Electrical Circuits*, Les Houches, Sessions LXIII, (1995)] and [B. Yurke and J. S. Denker, Phys. Rev. A. **29**, 1419, (1984)]). Quantization is achieved by elevating the node flux ϕ and charge q of the transmission line to quantum operators which generate the traveling fields. Below we bring into context the main results of such a description for the purposes in our paper and refer for further details to the references mentioned before.

The Hamiltonian of the transmission line reads:

$$\hat{H} = \int dz \left[\frac{\hat{q}^2(z, t)}{2c} + \frac{1}{2l} \left(\frac{\partial}{\partial z} \hat{\phi}(z, t) \right)^2 \right]. \quad (\text{S5})$$

The expression in square brackets is the Hamiltonian density of some element dz in the transmission line like suggested in Fig. S2 and the total Hamiltonian of the element is obtained by summing over all elements dz , yielding essentially the energy density in the transmission line, evaluated by the integral. Flux $\hat{\phi}$ across the inductor and charge density \hat{q} on the capacitor are conjugated variables and yield the voltages and currents on the transmission line; $\hat{\phi}(z, t) = \int_{-\infty}^t d\tau \hat{V}(z, \tau)$, $\hat{I}(z, t) = -\frac{1}{l} \frac{\partial \hat{\phi}(z, t)}{\partial z}$ and $c \frac{\partial \hat{\phi}}{\partial t} = c\hat{V}(z, t) = \hat{q}(z, t)$ with c and l being the capacitance and inductance per unit line length. Quantum mechanics enters the description of the transmission line by identifying *equal-time* commutation relations for the conjugated variables, $[\hat{\phi}(z, t), \hat{q}(z', t)] = i\hbar\delta(z - z')$ and $[\hat{q}(z', t), \hat{q}(z, t)] = [\hat{\phi}(z', t), \hat{\phi}(z, t)] = 0$ where we have taken the limit $dz \rightarrow 0$.

From the Hamiltonian equation of motion (or alternatively from the Euler-Lagrange equation) for the flux variable one finds that the flux obeys a 1D wave equation; $\frac{\partial^2 \hat{\phi}(z, t)}{\partial z^2} - \frac{1}{v_{ph}} \frac{\partial^2 \hat{\phi}(z, t)}{\partial z^2} = 0$ where $v_{ph} = \frac{1}{\sqrt{lc}}$ is the phase velocity. This form of wave equation can be interpreted as being a massless Klein-Gordon equation with the photon (excitation) on the transmission line being the fundamental particle.

The solution of the wave equation can be decomposed into an ingoing ('in') and an outgoing ('out') component where in Fig. S2 the 'in' part travels from positive z -coordinates towards '0' where the nonlinear oscillator is connected, and the 'out' part travels in the opposite direction towards the rest of the circuit and finally to the readout of the amplifier:

$$\begin{aligned} \hat{\phi}_{in}(z, t) &= \sqrt{\frac{\hbar}{2Y_c}} \int_0^\infty \frac{d\omega}{2\pi\sqrt{\omega}} \left(i\hat{a}_{in}[\omega] e^{-i\omega(t - \frac{z}{v_{ph}})} + \text{h.c.} \right) \\ \hat{\phi}_{out}(z, t) &= \sqrt{\frac{\hbar}{2Y_c}} \int_0^\infty \frac{d\omega}{2\pi\sqrt{\omega}} \left(i\hat{a}_{out}[\omega] e^{-i\omega(t + \frac{z}{v_{ph}})} + \text{h.c.} \right) \end{aligned} \quad (\text{S6})$$

In total $\hat{\phi} = \hat{\phi}_{in} + \hat{\phi}_{out}$ and 'h.c.' stands for the hermitian conjugate of the term in brackets. Note that the characteristic admittance can be written as $Y_c = \sqrt{c/l}$ and that there is a certain arbitrariness in the choice of the phase (yielding an extra 'i' and in certain cases also an extra sign in front of the equations) which has to be chosen in such a way to fulfill the operator commutation relations and to yield a consistent voltage on the transmission line. We will discuss this shortly.

In a next step one can formulate a quantized voltage. The in- and outgoing quantized voltages in the circuit at the point $z = 0$ then read (c.f. Fig. S2):

$$\begin{aligned} \hat{V}_{in}(t) &= \sqrt{\frac{\hbar}{2Y_c}} \int_0^\infty \frac{d\omega}{2\pi} \sqrt{\omega} \left(\hat{a}_{in}[\omega] e^{-i\omega t} + \text{h.c.} \right) \\ \hat{V}_{out}(t) &= \sqrt{\frac{\hbar}{2Y_c}} \int_0^\infty \frac{d\omega}{2\pi} \sqrt{\omega} \left(\hat{a}_{out}[\omega] e^{-i\omega t} + \text{h.c.} \right), \end{aligned} \quad (\text{S7})$$

and as before for the phase, also for the voltage $\hat{V} = \hat{V}_{in} + \hat{V}_{out}$. The charge density operator $\hat{q}_{in, out}$ on the transmission line is obtained by multiplying Eq. (S7) by the capacitance per unit line length c . Note that the creation and annihilation operators of the 'in' fields in frequency domain (\hat{a}_{in}^\dagger and \hat{a}_{in}) have a dimension of \sqrt{s} . Furthermore, they obey the following commutation relations (written below only for the 'in' operators):

$$\begin{aligned} [\hat{a}_{in}[\omega], \hat{a}_{in}[\omega']] &= [\hat{a}_{in}^\dagger[\omega], \hat{a}_{in}^\dagger[\omega']] = 0, \text{ and} \\ [\hat{a}_{in}[\omega], \hat{a}_{in}^\dagger[\omega']] &= 2\pi\delta(\omega - \omega'). \end{aligned} \quad (\text{S8})$$

The 'in' and 'out' fields do always commute with each other (for instance $[\hat{a}_{in}[\omega], \hat{a}_{out}^\dagger[\omega']] = 0$). As a quick sanity check, we verify whether the results Eq. (S6)-(S8) fulfill the commutation relations for the conjugated variables $\hat{\phi}$ and \hat{q} . The commutator for the flux and charge density reads:

$$\begin{aligned} \left[\hat{\phi}(z, t), \hat{q}(z', t) \right] = & \hat{\phi}_{in}(z, t)\hat{q}_{in}(z', t) + \hat{\phi}_{in}(z, t)\hat{q}_{out}(z', t) + \hat{\phi}_{out}(z, t)\hat{q}_{in}(z', t) + \hat{\phi}_{out}(z, t)\hat{q}_{out}(z', t) \\ & - \hat{q}_{in}(z', t)\hat{\phi}_{in}(z, t) - \hat{q}_{in}(z', t)\hat{\phi}_{out}(z, t) - \hat{q}_{out}(z', t)\hat{\phi}_{in}(z, t) - \hat{q}_{out}(z', t)\hat{\phi}_{out}(z, t), \end{aligned} \quad (\text{S9})$$

where the mixed 'in/out' operator products are zero according to the commutation relations for the fields,

Eq. (S8). Finally, we are left with the following expression which consists of four main terms (i)-(iv):

$$\underbrace{\hat{\phi}_{in}(z, t)\hat{q}_{in}(z', t)}_{(i)} + \underbrace{\hat{\phi}_{out}(z, t)\hat{q}_{out}(z', t)}_{(ii)} - \underbrace{\hat{q}_{in}(z', t)\hat{\phi}_{in}(z, t)}_{(iii)} - \underbrace{\hat{q}_{out}(z', t)\hat{\phi}_{out}(z, t)}_{(iv)}. \quad (\text{S10})$$

The difference between term (i) and term (iii) yields half

the value of the commutator in Eq. (S9):

$$\begin{aligned} \hat{\phi}_{in}(z, t)\hat{q}_{in}(z', t) - \hat{q}_{in}(z', t)\hat{\phi}_{in}(z, t) &= c \frac{i\hbar}{8\pi^2 Y_c} \int_{\mathcal{D}} d\omega' d\omega \left\{ \left(\hat{a}_{in}[\omega] e^{-i\omega(t - \frac{z}{v_{ph}})} \hat{a}_{in}^\dagger[\omega'] e^{+i\omega'(t - \frac{z'}{v_{ph}})} \right) \right. \\ &- \left(\hat{a}_{in}^\dagger[\omega] e^{+i\omega(t - \frac{z}{v_{ph}})} \hat{a}_{in}[\omega'] e^{-i\omega'(t - \frac{z'}{v_{ph}})} \right) + \left(\hat{a}_{in}[\omega'] e^{-i\omega'(t - \frac{z'}{v_{ph}})} \hat{a}_{in}^\dagger[\omega] e^{+i\omega(t - \frac{z}{v_{ph}})} \right) \\ &- \left. \left(\hat{a}_{in}^\dagger[\omega'] e^{+i\omega'(t - \frac{z'}{v_{ph}})} \hat{a}_{in}[\omega] e^{-i\omega(t - \frac{z}{v_{ph}})} \right) \right\} \\ &= c \frac{i\hbar}{8\pi^2 Y_c} \int_{\mathcal{D}} d\omega' d\omega \left\{ \left[\hat{a}_{in}[\omega], \hat{a}_{in}^\dagger[\omega'] \right] e^{-i(\omega - \omega')t - i(\omega' \frac{z'}{v_{ph}} - \omega \frac{z}{v_{ph}})} + \left[\hat{a}_{in}[\omega'], \hat{a}_{in}^\dagger[\omega] \right] e^{-i(\omega' - \omega)t - i(\omega \frac{z}{v_{ph}} - \omega' \frac{z'}{v_{ph}})} \right\} \\ &= c \frac{i\hbar}{8\pi^2 Y_c} \int_{\mathcal{D}} d\omega' d\omega \left\{ 2\pi\delta(\omega - \omega') e^{-i(\omega - \omega')t - i(\omega' \frac{z'}{v_{ph}} - \omega \frac{z}{v_{ph}})} + 2\pi\delta(\omega' - \omega) e^{-i(\omega' - \omega)t - i(\omega \frac{z}{v_{ph}} - \omega' \frac{z'}{v_{ph}})} \right\} \\ &= \frac{i\hbar}{4\pi v_{ph}} \int_{0^-}^{\infty} d\omega \left\{ e^{-i\frac{\omega}{v_{ph}}(z' - z)} + e^{-i\frac{\omega}{v_{ph}}(z - z')} \right\} = \frac{i\hbar}{2} \int_{0^-}^{\infty} \frac{dk}{2\pi} \left\{ e^{-ik(z' - z)} + e^{-ik(z - z')} \right\} = \frac{i\hbar}{2} \delta(z - z'), \end{aligned} \quad (\text{S11})$$

where in the last steps we have expressed $\omega = v_{ph}k$ with k being the wave vector. Also, we have already taken into account that equal pairs of creation and annihilation operators for the fields are equal to zero (c.f. Eq. (S8)) and the integration contour \mathcal{D} is for now the positive \mathbb{R}^2 .

We obtain the same result like in Eq. (S11) for the difference between the terms (ii) and (iv) in Eq. (S10) and have, therefore, verified that the commutation relation for the flux and charge density are correct and, consequently, also the relations Eq. (S6) and Eq. (S7).

The equal pair commutation relations $[\hat{\phi}(z, t), \hat{\phi}(z', t)] = 0$ and $[\hat{q}(z, t), \hat{q}(z', t)] = 0$ are trivially fulfilled which is obtained by a similar calculation like the one before.

We further assume the following Fourier relations for

the annihilation and creation operators:

$$\begin{aligned} \hat{a}_{in}(t) &= \int_{-\infty}^{\infty} \frac{d\omega}{2\pi} \hat{a}_{in}[\omega] e^{-i\omega t} \\ \hat{a}_{in}[\omega] &= \int_{-\infty}^{\infty} dt \hat{a}_{in}(t) e^{+i\omega t} \\ \hat{a}_{in}^\dagger(t) &= \int_{-\infty}^{\infty} \frac{d\omega}{2\pi} \hat{a}_{in}^\dagger[\omega] e^{-i\omega t} \\ \hat{a}_{in}^\dagger[\omega] &= \int_{-\infty}^{\infty} dt \hat{a}_{in}^\dagger(t) e^{+i\omega t}, \end{aligned} \quad (\text{S12})$$

and correspondingly for the 'out' fields, following the convention suggested in [A. A. Clerk et al., Rev. Mod. Phys. **82**, 1155, 2010]. Note that in this convention the sign of the exponentials of the time or frequency \hat{a} and \hat{a}^\dagger operators is the same in contrast to the definition which is usually used in quantum optics where the signs are opposite. The practical reason for our defi-

inition of these operators is that one can express now two different frequency modes (for us this is the signal and idler mode of the JPA) by specifying either $\hat{a}[\omega]$ (signal) or $(\hat{a}[-\omega])^\dagger = \hat{a}^\dagger[\omega]$ (idler) as described by [A. A. Clerk et al., Rev. Mod. Phys. **82**, 1155, 2010].

With the definitions Eq. (S12) one obviously transforms also the fields \hat{V} , $\hat{\phi}$ and \hat{q} from time into frequency domain and back with the same sign convention as discussed before.

Sometimes it is easier to interpret fields of the form like in Eq. (S7) by going over to the Markov approximation in which one assumes a sharp enough frequency response of the nonlinear oscillator around its plasma frequency ω_0 . One obtains then:

$$\hat{V}_{in}(t) = \sqrt{\frac{\hbar\omega_0}{2Y_c}} \left(\hat{a}_{in}(t)e^{-i\omega_0 t} + \hat{a}_{in}^\dagger(t)e^{+i\omega_0 t} \right), \quad (\text{S13})$$

and corresponding equations for the other fields. In this case, however, the interpretation of the creation and annihilation fields is different and they represent now slow varying envelopes compared to the oscillation frequency ω_0 of the nonlinear oscillator.

With this preparation at hand, a spatially dependent admittance on a transmission line can then be defined as:

$$Y[z, \omega] = \frac{I[z, \omega]}{V[z, \omega]} = (Z[z, \omega])^{-1}, \quad (\text{S14})$$

which allows in turn to define a reflection coefficient (in essence the ratio between in- and output fields):

$$r[z, \omega] = \frac{Z[z, \omega] - Z_c}{Z[z, \omega] + Z_c}, \quad (\text{S15})$$

with $Z_c = Y_c^{-1}$ being the characteristic impedance of the transmission line on which the reflection coefficient is measured. The reflection coefficient can obviously also be defined as $V_{out} = rV_{in}$. By the choice of the symbol 'r' instead of 'T' which is usually used in classical microwave theory to express the reflection coefficient, we choose a formalism used to describe parametric amplifiers in the input-output formalism.

Having a language defined how we can describe a circuit quantum mechanically, we come back to formulate a nonlinear oscillator equation describing pumping through a weak quantum signal send into the oscillator via the (quantum) transmission line which is connected to it.

The current in the circuit $\hat{I}(z, t) = Y_c \left(\hat{V}_{in}(z, t) - \hat{V}_{out}(z, t) \right)$, shown in Fig. S2, has to obey *Kirchhoff's* law and we will focus now on the point $z = 0$ which is the point at which the transmission line connects to the nonlinear oscillator:

$$\begin{aligned} -\hat{I}(t) + \hat{I}_L(t) + \hat{I}_C(t) &= 0 \\ \Rightarrow \hat{I}_L(t) + Y_{in}''''\hat{V}(t) + \hat{I}_C(t) &= 2Y_{in}''''\hat{V}_{in}(t), \end{aligned} \quad (\text{S16})$$

where we have written $\hat{V}_{out}(t) = \hat{V}(t) - \hat{V}_{in}(t)$ and explicitly identified the input admittance Y_{in}'''' at the point $z = 0$ of the transmission line in consistence to the notation we use in the main text. At the same time this admittance, however, is to good approximation equal to the characteristic admittance of the transmission line over the operation bandwidth of the parametric amplifier but leaves space for a more general description of the circuit since it carries a real and a complex part which is tunable by our circuit design. The right side of Eq. (S16) is the pumping term of the nonlinear oscillator due to a weak (quantum signal). Going back to Eq. (S2) we can write the total pumping term $I(t)$ then as:

$$I(t) = \bar{I}_p \cos(\omega_p t) + 2Y_{in}''''\hat{V}_{in}(t) = \bar{I}_p \cos(\omega_p t) + 2\hat{I}_{in}(t), \quad (\text{S17})$$

consisting of a classical pump tone and the weak quantum signal (\hat{I}_{in}). Therefore, the equation describing the nonlinear oscillator, pumped by a classical source and a quantum signal can be written as:

$$\begin{aligned} \ddot{\delta}(t) + \frac{Y_{in}''''}{C_0}\dot{\delta}(t) + \omega_0^2 \left[\delta(t) - \frac{1}{6}\delta(t)^3 \right] - \omega_0^2 \frac{\bar{I}_p \cos(\omega_p t)}{I_c(\Phi)} \\ = \frac{4\pi\hat{I}_{in}(t)}{\phi_0 C_0}. \end{aligned} \quad (\text{S18})$$

Note that the phase δ contains now the two components introduced already at the beginning of this supplemental information, the classical component δ_p which we summarize for different pumping strengths in Fig. S1 and the quantum (or weak signal) component $\hat{\delta}_s$ which will be the subject of our further discussion and the central variable to calculate the parametric gain.

Since $\hat{\delta}_s \ll \delta_p$, it can be treated as a small perturbation around the solution of the strong pump δ_p . To first order the solution reads then $\delta = \delta_p + \hat{\delta}_s$ which is nothing more than a first order perturbation expansion of $\hat{\delta}_s$ around the large-signal solution of the nonlinear oscillator which we have already solved before.

We substitute $\delta(t) = \delta_p(t) + \hat{\delta}_s(t)$ into Eq. (S18) and retain only linear terms in $\hat{\delta}_s(t)$. Furthermore, we subtract the large signal equation of motion (i.e. the equation of motion for the classical phase δ_p) from the equation of motion of δ (Eq. (S18)) in order to obtain the equation of motion describing the dynamics of the intra-oscillator quantum variable $\hat{\delta}_s(t)$. We finally obtain:

$$\ddot{\delta}_s(t) + \frac{Y_{in}''''}{C_0} \dot{\delta}_s(t) + \omega_0^2 \left\{ 1 - \frac{\delta_{p,max}^2}{4} [\cos(2\omega_p t - 2\varphi) + 1] \right\} \delta_s(t) = \frac{4\pi \hat{I}_{in}(t)}{\phi_0 C_0} = \frac{4\pi Y_{in}'''' \hat{V}_{in}(t)}{\phi_0 C_0}. \quad (\text{S19})$$

In the argument of the $\cos(\cdot)$ -term, we recall that the φ -term is related to the in-phase and quadrature terms of the large signal solution, cf. Eq. (S3). Also, we write for the intra-oscillator fields:

$$\begin{aligned} \hat{\delta}_s(t) &= \int_0^\infty \frac{d\omega}{2\pi} \left(\hat{\delta}_s[\omega] e^{-i\omega t} + \hat{\delta}_s^\dagger[\omega] e^{+i\omega t} \right) \text{ and} \\ \hat{\delta}_s[\omega] &= \int_0^\infty dt \left(\hat{\delta}_s(t) e^{+i\omega t} + \hat{\delta}_s^\dagger(t) e^{-i\omega t} \right) \end{aligned} \quad (\text{S20})$$

at the point $z = 0$ of the circuit shown in Fig. S2. We

will show further below how the intra-oscillator field $\hat{\delta}_s$ is connected to the in- and output fields via the input-output formalism.

Our goal is now to go over to the frequency domain representation of Eq. (S19). Fourier transformation of Eq. (S19) yields the following equation of motion in the frequency domain at the point $z = 0$ in the circuit shown in Fig. S2:

$$\begin{aligned} \left[-\omega^2 - i\omega\kappa[\omega] + \omega_0^2 \left(1 - \frac{\delta_{p,max}^2}{4} \right) \right] \hat{\delta}_s[\omega] - \frac{\omega_0^2 \delta_{p,max}^2}{8} e^{+i2\varphi} \hat{\delta}_s^\dagger[-\omega + 2\omega_p] &= \frac{4\pi Y_{in}''''[\omega] \hat{V}_{in}[\omega]}{\phi_0 C_0} \\ &= \frac{4\pi\kappa[\omega]}{\phi_0} \sqrt{\frac{\hbar\omega}{2Y_{in}''''[\omega]}} \hat{a}_{in}[\omega]. \end{aligned} \quad (\text{S21})$$

In detail, we use the Fourier convolution theorem to ob-

tain the Fourier transformation of the term containing the $\cos(\cdot)$ function in Eq. (S19):

$$\begin{aligned} \mathcal{F} \left[\hat{\delta}_s(t) \cdot \cos(2\omega_p t - 2\varphi) \right] &= \mathcal{F} \left[\hat{\delta}_s(t) \right] * \mathcal{F} \left[\cos(2\omega_p t - 2\varphi) \right] \\ &= \frac{1}{2} \int_{-\infty}^{\infty} d\omega' \hat{\delta}_s[\omega'] \left(e^{+i2\varphi} \delta_{Dirac}[-2\omega_p + \omega - \omega'] + e^{-i2\varphi} \delta_{Dirac}[+2\omega_p + \omega - \omega'] \right) \\ &= \frac{1}{2} \left(e^{+i2\varphi} \hat{\delta}_s[\omega - 2\omega_p] + e^{-i2\varphi} \hat{\delta}_s[\omega + 2\omega_p] \right) \\ &= \frac{1}{2} \left(e^{+i2\varphi} \hat{\delta}_s^\dagger[-\omega + 2\omega_p] + e^{-i2\varphi} \hat{\delta}_s^\dagger[-\omega - 2\omega_p] \right) \\ &\approx \frac{1}{2} e^{+i2\varphi} \hat{\delta}_s^\dagger[-\omega + 2\omega_p]. \end{aligned} \quad (\text{S22})$$

Here, $\mathcal{F}[\cdot]$ denotes the Fourier transform, $*$ is the symbol for the convolution product and $\delta_{Dirac}(\cdot)$ is the Dirac distribution. For the transformation $\hat{\delta}_s \rightarrow \hat{\delta}_s^\dagger$ we use the definitions (S12) for the operators and Eq. (S20). In order to obtain the last expression in Eq. (S22) we recognize that the second term $\propto \hat{\delta}_s^\dagger[-\omega - 2\omega_p]$ decays much faster than the first term. In Eq. (S21) we identify also $\kappa = (Y_{in}''''[\omega]/C_0)$ being the damping rate introduced by the nonlinear oscillator. Note that only the field \hat{a}_{in} appears on the right side of the equation, because we assume without loss of generality that we inject a tone on the signal side (not on the idler side) of the input field. Similarly one could describe an input tone injected on the

idler side by considering the adjoint of the same equation. This we will describe in more detail further below. Recalling again the dimension of \hat{a}_{in} of \sqrt{s} , the right side side of Eq. (S21) has the dimension $1/s$, like the left side. Exclusively for the Fourier transformation of Eq. (S19) we use the convention $f(t) = \int d\omega F(\omega) \exp(-i\omega t)$ and $F(\omega) = 1/(2\pi) \int dt f(t) \exp(+i\omega t)$ bringing the expression (S21) to a tractable form.

From now on we will identify $\omega = \omega_s$, where ω_s is the signal frequency and we will use the symbol ω_i to denote the idler frequency of the parametric amplifier. Equally we will use the indices 's' and 'i' to label some operators we will use in the following which act on the signal and

idler frequencies.

Our goal is now to bring Eq. (S21) into a form which is compatible with the input-output formalism. In particular Eq. (S21) should assume a form which allows us to compare it with the input-output relation for a simple harmonic oscillator (without nonlinearity from a Josephson junction or other nonlinear elements), which we would like to use for a sanity check and to highlight the effect of the nonlinearity in our system.

We proceed to rewrite Eq. (S21) by performing a rotating-wave-approximation so that the equation ro-

tates approximately at the pump frequency. For this we also apply the following substitutions, $\omega_p + \omega_s \approx 2\omega_p$ and also $\omega_s/\omega_0 \approx 1$. This means essentially also that around the resonator's plasma frequency we can assume that $\omega_s \approx \omega_p \approx \omega_0$ to good approximation.

We first divide Eq. (S21) by ω_0 and then add and subtract the adequate amount of frequencies so that at the end we can divide by the factor of '2' in front of the term proportional to $\kappa[\omega]$ on the left side of Eq (S21) without introducing artificially fractions of frequencies. We obtain then:

$$\begin{aligned}
& \left[-\omega_s^2 - i\omega_s\kappa[\omega_s] + \omega_0^2 \left(1 - \frac{\delta_{p,max}^2}{4} \right) \right] \hat{\delta}_s[\omega_s]e^{-i\varphi} - \frac{\omega_0^2\delta_{p,max}^2}{8} \hat{\delta}_s^\dagger[-\omega_s + 2\omega_p]e^{+i\varphi} = \frac{4\pi\kappa[\omega_s]}{\phi_0} \sqrt{\frac{\hbar\omega_s}{2Y_{in}''''[\omega_s]}} \hat{a}_{in}[\omega_s]e^{-i\varphi} \\
\Rightarrow & \left[\omega_0 - \omega_s - \frac{\omega_0\delta_{p,max}^2}{4} - i\kappa[\omega_s] \right] \hat{\delta}_s[\omega_s]e^{-i\varphi} - \frac{\omega_0\delta_{p,max}^2}{8} \hat{\delta}_s^\dagger[-\omega_s + 2\omega_p]e^{+i\varphi} = \frac{4\pi\kappa[\omega_s]}{\phi_0\omega_0} \sqrt{\frac{\hbar\omega_s}{2Y_{in}''''[\omega_s]}} \hat{a}_{in}[\omega_s]e^{-i\varphi} \\
\Rightarrow & \left[2\tilde{\omega}_p - 2\tilde{\omega}_s - \frac{\omega_0\delta_{p,max}^2}{4} - i\kappa[\tilde{\omega}_s] \right] \hat{\delta}_s[\tilde{\omega}_s]e^{-i\varphi} - \frac{\omega_0\delta_{p,max}^2}{8} \hat{\delta}_s^\dagger[-\tilde{\omega}_s]e^{+i\varphi} = \frac{4\pi\kappa[\tilde{\omega}_s]}{\phi_0\omega_0} \sqrt{\frac{\hbar\omega_s}{2Y_{in}''''[\tilde{\omega}_s]}} \hat{a}_{in}[\tilde{\omega}_s]e^{-i\varphi} \\
\Rightarrow & \left[\tilde{\omega}_p - \tilde{\omega}_s - \frac{\omega_0\delta_{p,max}^2}{8} - \frac{i\kappa[\tilde{\omega}_s]}{2} \right] \hat{\delta}_s[\tilde{\omega}_s]e^{-i\varphi} - \frac{\omega_0\delta_{p,max}^2}{16} e^{+i\varphi} \hat{\delta}_s^\dagger[-\tilde{\omega}_s] = \frac{2\pi\kappa[\tilde{\omega}_s]}{\phi_0\omega_0} \sqrt{\frac{\hbar\omega_s}{2Y_{in}''''[\tilde{\omega}_s]}} \hat{a}_{in}[\tilde{\omega}_s]e^{-i\varphi} \\
\Rightarrow & \left[i(\tilde{\Omega}_p - \tilde{\omega}_s) + \frac{\kappa[\tilde{\omega}_s]}{2} \right] \hat{\delta}_s[\tilde{\omega}_s]e^{-i\varphi} - \frac{i\omega_0\delta_{p,max}^2}{16} e^{+i\varphi} \hat{\delta}_s^\dagger[-\tilde{\omega}_s] = i \frac{2\pi\kappa[\tilde{\omega}_s]}{\phi_0\omega_0} \sqrt{\frac{\hbar\omega_s}{2Y_{in}''''[\tilde{\omega}_s]}} \hat{a}_{in}[\tilde{\omega}_s]e^{-i\varphi}.
\end{aligned} \tag{S23}$$

We use in the derivation above the notation for the pump and signal detuning, indicated by a *tilde* like in the main text and as mentioned in the beginning of this supplemental information; $\tilde{\omega}_p = \omega_0 - \omega_p$ and $\tilde{\omega}_s = \omega_p - \omega_s$. We denote the effective parametric pump frequency with a capital $\tilde{\Omega}_p$ since it contains the pump frequency detuning $\tilde{\omega}_p$ and the additional term $-\omega_0\delta_{p,max}^2/8$, leading to the frequency shift we have already shown in Fig. S1; $\tilde{\Omega}_p = \tilde{\omega}_p - \omega_0\delta_{p,max}^2/8$. This is a typical characteristic of a nondegenerate parametric amplifier in which one pumps a Kerr-type nonlinearity through the signal port; the oscillator response shifts when the pumping power increases. This has to be taken into account during the operation of the device and an amplifier design is desired where this effect is minimal.

Note also that the negative frequency argument in the expression $\hat{\delta}_s^\dagger[-\tilde{\omega}_s]$ means that a photon on the idler side is created with frequency $\omega_i = 2\omega_p - \omega_s$ and $\tilde{\omega}_s \geq 0$.

We now go over to creation and annihilation fields by applying the following identities to Eq. (S23), compatible with the input-output formalism as described by [A. A. Clerk et al., Rev. Mod. Phys. **82**, 1155, (2010)]; $\hat{a}_s[\tilde{\omega}_s] = \hat{\delta}_s[\tilde{\omega}_s]e^{-i\varphi}$, $\hat{a}_i[-\tilde{\omega}_s] = \hat{\delta}_s^\dagger[-\tilde{\omega}_s]e^{+i\varphi}$ and $i \frac{2\pi\kappa[\tilde{\omega}_s]}{\phi_0\omega_0} \sqrt{\frac{\hbar\omega_s}{2Y_{in}''''[\tilde{\omega}_s]}} \hat{a}_{in}[\tilde{\omega}_s]e^{-i\varphi} \rightarrow \hat{a}_{in}[\tilde{\omega}_s]$, where now the indices s and i of the intra-oscillator fields \hat{a}, \hat{a}^\dagger label

specifically the signal (s) and idler (i) modes. Note that after these variable transformations, \hat{a}_{in} is dimensionless, whereas the intra-oscillator fields obtain a dimension of s .

Equation (S23) then assumes the simple form:

$$\left[i(\tilde{\Omega}_p - \tilde{\omega}_s) + \frac{\kappa[\tilde{\omega}_s]}{2} \right] \hat{a}_s[\tilde{\omega}_s] - \frac{i\omega_0\delta_{p,max}^2}{16} \hat{a}_i^\dagger[-\tilde{\omega}_s] = \hat{a}_{in}[\tilde{\omega}_s]. \tag{S24}$$

Together with its adjoint (effectively this interchanges the role of signal and idler terms):

$$\begin{aligned}
\left[-i(\tilde{\Omega}_p + \tilde{\omega}_s) + \frac{\kappa^*[-\tilde{\omega}_s]}{2} \right] \hat{a}_i^\dagger[-\tilde{\omega}_s] + \frac{i\omega_0\delta_{p,max}^2}{16} \hat{a}_s[\tilde{\omega}_s] \\
= \hat{a}_{in}^\dagger[-\tilde{\omega}_s], \tag{S25}
\end{aligned}$$

where again $\tilde{\omega}_s \geq 0$. We obtain all coefficients necessary to build up the susceptibility matrix for the parametric amplifier. This matrix is needed for the description of the parametric amplifier in the framework of the input-output formalism which is briefly sketched in the following section and which we have heavily condensed for the purposes in this paper.

**INPUT-OUTPUT FORMALISM AND QUANTUM
NOISE FOR A NONDEGENERATE (PHASE
PRESERVING) JPA**

With the previous preparation at hand we formulate a relation which connects the intra-oscillator field $\hat{\mathbf{a}} = (\hat{a}_s[\tilde{\omega}_s], \hat{a}_i^\dagger[-\tilde{\omega}_s])^T$ with the input field $\hat{\mathbf{a}}_{in} = (\hat{a}_{in}[\tilde{\omega}_s], \hat{a}_{in}^\dagger[-\tilde{\omega}_s])^T$ in consistence with the work done by [A. A. Clerk et al., Rev. Mod. Phys. **82**, 1155, (2010); C. Laflamme and A. A. Clerk, Phys. Rev. A **83**, 033803, (2011); Tanay Roy et al., Appl. Phys. Lett. **107**, 262601, (2015); R. Vijay et al., Rev. Sci. Instrum. **80**, 111101, (2009) and V. E. Manucharyan et al. Phys. Rev. B **76**, 014524, (2007)]:

$$\chi[\tilde{\omega}_s]^{-1} \cdot \hat{\mathbf{a}}[\tilde{\omega}_s] = \hat{\mathbf{a}}_{in}[\tilde{\omega}_s]. \quad (\text{S26})$$

The inverted susceptibility matrix [A. A. Clerk et al., Rev. Mod. Phys. **82**, 1155, (2010); C. Laflamme and A. A. Clerk, Phys. Rev. A **83**, 033803, (2011)] reads:

$$\chi[\tilde{\omega}_s]^{-1} = -i \begin{pmatrix} [-(\tilde{\Omega}_p - \tilde{\omega}_s) + \frac{i\kappa[\tilde{\omega}_s]}{2}] & \frac{\omega_0 \delta_{p,max}^2}{16} \\ -\frac{\omega_0 \delta_{p,max}^2}{16} & [(\tilde{\Omega}_p + \tilde{\omega}_s) + \frac{i\kappa^*[-\tilde{\omega}_s]}{2}] \end{pmatrix}, \quad (\text{S27})$$

being the coefficient matrix of the equation system (S24) and (S25). As mentioned in the previous section, we now want to compare the susceptibility (S27) with the one for an one-sided empty oscillator without nonlinearity. In this case we find a similar susceptibility just without off-diagonal entries which are on the other hand indispensable in parametric amplification in order to enable energy exchange between the frequency modes.

Following the theory in [A. A. Clerk et al., Rev. Mod. Phys. **82**, 1155, (2010); C. Laflamme and A. A. Clerk, Phys. Rev. A **83**, 033803, (2011)] the photon number gain (or power gain) of the signal mode of the parametric amplifier can then be evaluated by evaluating the following relation:

$$G_s[\tilde{\omega}_s] = |1 - \kappa[\tilde{\omega}_s]\chi_{11}[\tilde{\omega}_s]|^2, \quad (\text{S28})$$

and the photon number gain of the idler mode reads:

$$G_i[-\tilde{\omega}_s] = |1 - \kappa[-\tilde{\omega}_s]\chi_{11}[-\tilde{\omega}_s]|^2. \quad (\text{S29})$$

For the evaluation, we numerically invert (S27) for each detuning $\tilde{\omega}_s$ and subsequently substitute the matrix element χ_{11} into the equations (S28) and (S29). For a symmetric admittance function around $\tilde{\omega}_s$ like in our work we obviously find $G_s = G_i$. Asymmetries are introduced by other imperfections of the circuit which we detail in the main text.

While the susceptibility matrix (S27) connects the intra-oscillator with the input field, yielding the gain of the parametric amplifier, supplemental input-output relations connect further the input fields with the output

(amplified) fields:

$$\begin{pmatrix} \hat{a}_{out}[\tilde{\omega}_s] \\ \hat{a}_{out}^\dagger[-\tilde{\omega}_s] \end{pmatrix} = \begin{pmatrix} \mathcal{G}[\tilde{\omega}_s] & \mathcal{M}[\tilde{\omega}_s] \\ \mathcal{M}^*[-\tilde{\omega}_s] & \mathcal{G}^*[-\tilde{\omega}_s] \end{pmatrix} \begin{pmatrix} \hat{a}_{in}[\tilde{\omega}_s] \\ \hat{a}_{in}^\dagger[-\tilde{\omega}_s] \end{pmatrix}. \quad (\text{S30})$$

This gain relation of an idealized and initially lossless nondegenerate parametric amplifier is of particular importance to understand the minimum noise which is added by a real amplifier and will lead to the fundamental result of the Haus-Caves theorem [H. A. Haus and J. A. Mullen, Phys. Rev. **128**, 2407, (1962); C. C. Caves, Phys. Rev. D **26**, 1817, (1982)].

Here, the calligraphic letters in the gain matrix denote the amplitude gain instead of the power gain which is on the other hand evaluated by Eqs. (S28) and (S29). Specifically, $\mathcal{G}[\tilde{\omega}_s]$ denotes the amplitude gain at the signal frequency whereas $\mathcal{M}[-\tilde{\omega}_s]$ denotes the amplitude conversion gain at the idler frequency for a frequency being injected into the parametric amplifier at the signal frequency $\tilde{\omega}_s$.

The following identities are needed for the further presentation:

$$\begin{aligned} |\mathcal{G}[\pm\tilde{\omega}_s]|^2 - |\mathcal{M}[\pm\tilde{\omega}_s]|^2 &= 1 \\ \text{and} & \\ \mathcal{G}[\tilde{\omega}_s]\mathcal{M}[-\tilde{\omega}_s] &= \mathcal{G}[-\tilde{\omega}_s]\mathcal{M}[\tilde{\omega}_s]. \end{aligned} \quad (\text{S31})$$

The power gain can then be expressed via the amplitude gain as $G_s[\tilde{\omega}_s] = |\mathcal{G}[\tilde{\omega}_s]|^2$ and $G_i[-\tilde{\omega}_s] = |\mathcal{M}[\tilde{\omega}_s]|^2$ and $G_i[-\tilde{\omega}_s] = G_s[\tilde{\omega}_s] - 1$. Clearly, for large power gains $\gg 1$, $G_s \approx G_i$.

We now go over to an equation like Eq. (S30) including noise and want to focus on the ground state of the electromagnetic field. By this we determine the minimum noise the nondegenerate parametric amplifier will add to the signal referred to the input. For this we will consider a blackbody load at temperature $k_B T \ll \hbar\omega_p$, i.e. close to its ground state, injecting power into the parametric amplifier and we calculate the power spectral density at its output.

The first component of Eq. (S30) reads $\hat{a}_{out}[\tilde{\omega}_s] = \mathcal{G}[\tilde{\omega}_s]\hat{a}_{in}[\tilde{\omega}_s] + \mathcal{M}[\tilde{\omega}_s]\hat{a}_{in}^\dagger[-\tilde{\omega}_s]$ and shows two important properties of a nondegenerate JPA. First, signal and idler modes are strongly correlated since $\mathcal{G} \approx \mathcal{M}$ for high gains and, second, noise from the idler is added to the signal portion of the amplified signal. We will be more specific on the second property now.

In order to simplify the following discussion, we use the fact that a nondegenerate JPA does not favor the amplification/de-amplification of a particular signal quadrature, rather it treats both quadratures equally and independent of the input signal phase shift with respect to the pump tone.

The total noise of the JPA at its output with respect to its input (compare with Fig. S2) can be expressed by quantifying the fluctuations of the input field and how they are transformed into the output field. We write the first component of Eq. (S30) in terms of noise power

spectral densities of the input signal and idler and of the output fields and obtain:

$$\begin{aligned}
S_{out}[\tilde{\omega}_s] &= G_s[\tilde{\omega}_s]\mathcal{S}_{in}[\tilde{\omega}_s] + G_i[-\tilde{\omega}_s]\mathcal{S}_{in}[-\tilde{\omega}_s] \\
&= G_s[\tilde{\omega}_s]\mathcal{S}_{in}[\tilde{\omega}_s] + (G_s[\tilde{\omega}_s] - 1)\mathcal{S}_{in}[-\tilde{\omega}_s] \\
&= G_s[\tilde{\omega}_s]\frac{\hbar\omega_p}{2}\left(\langle\hat{a}_{in}[\tilde{\omega}_s]\hat{a}_{in}^\dagger[\tilde{\omega}_s]\rangle + \langle\hat{a}_{in}^\dagger[\tilde{\omega}_s]\hat{a}_{in}[\tilde{\omega}_s]\rangle\right) + (G_s[\tilde{\omega}_s] - 1)\frac{\hbar\omega_p}{2}\left(\langle\hat{a}_{in}[-\tilde{\omega}_s]\hat{a}_{in}^\dagger[-\tilde{\omega}_s]\rangle + \langle\hat{a}_{in}^\dagger[-\tilde{\omega}_s]\hat{a}_{in}[-\tilde{\omega}_s]\rangle\right) \\
&= G_s[\tilde{\omega}_s]\frac{\hbar\omega_p}{2}\coth\left(\frac{\hbar\omega_p}{2k_B T}\right) + (G_s[\tilde{\omega}_s] - 1)\frac{\hbar\omega_p}{2}\coth\left(\frac{\hbar\omega_p}{2k_B T}\right) \\
&= G_s[\tilde{\omega}_p]\left\{\frac{\hbar\omega_p}{2}\coth\left(\frac{\hbar\omega_p}{2k_B T}\right) + \left(1 - \frac{1}{G_s[\tilde{\omega}_s]}\right)\frac{\hbar\omega_p}{2}\coth\left(\frac{\hbar\omega_p}{2k_B T}\right)\right\}.
\end{aligned} \tag{S32}$$

where as said before, the G 's are the power gains. Also we assume that the signal and idler frequencies are close enough to the pump frequency ω_p so that we can develop the noise spectral densities around ω_p without introducing too large errors. By considering the small change of the $\coth(\cdot)$ -terms in the -3 dB bandwidth of our amplifier this approximation is obviously valid for our case. The last line of Eq. (S32) is the fundamental result of the Haus-Caves theorem for a nondegenerate JPA (or in other words a phase-preserving amplifier), which for gains $\gg 1$ will add a minimum amount of shot noise equivalent to half a photon per second per Hertz of bandwidth to the amplified portion of the signal at the input. In total, together with the vacuum fluctuation in the signal input field, the nondegenerate JPA will amplify at least a shot noise equivalent to one photon per second per Hertz of bandwidth at its input which is added to the desired signal in the input field.

For a real device, the noise as a function of the signal frequency is not flat which on the other hand is suggested by Eq. (S32). The gain profile, the coupling to the device, the shape of the input admittance function $Y_{in}''''[\tilde{\omega}_s]$ and possible losses in the signal path will contribute to the total noise with respect to the input and will increase the minimum noise amount suggested by Eq. (S32). We describe this in detail in the main text for our device.

BROADBAND DIELECTRIC LOADED COPLANAR WAVEGUIDE-TO-MICROSTRIP TRANSFORMER FOR QUANTUM CIRCUITS

In this section we provide design dimensions and simulation results obtained with CST microwave studio [CST-Computer Simulation Technology, <https://www.cst.com>] for an ultra broadband dielectric loaded coplanar waveguide (CPW)-to-microstrip (MS) transformer circuit. With such a transformer, one could connect our microstrip amplifier to a CPW structure, either for connection to the input/output cabling or to other quantum circuits which are often designed using CPW geometries.

Figures S3 and S4 present our results. Both ports '1' and '2' have a characteristic impedance of 50Ω .

DISPERSION RELATION ON A SUPERCONDUCTING AL MICROSTRIP TRANSMISSION LINE

We employ aluminum based superconducting microstrip (MS) transmission lines in our device. It is known that the geometrical length corresponding to some electrical length on such a transmission line (and in principle no matter which material is employed) is shorter than in its normal conducting state [D. C. Mattis and J. Bardeen, Phys. Rev. **111**, 412, (1958); R. L. Kautz, J. Appl. Phys. **49**, 308, (1978)]. The fundamental reason for this is that the phase velocity slows down when the material becomes superconducting [R. L. Kautz, J. Appl. Phys. **49**, 308, (1978)] and to compensate for that one has to shorten the transmission line. There are three leading influences how strong the dispersion relation, and therefore the phase velocity, is modified in the superconducting state of the MS transmission line compared to its normal-state value.

First, the geometry of the MS transmission line, in particular the ratio between MS conductor width W and dielectric thickness d , second, the normal state resistivity ρ_n (measured for Al at 77 K) and finally the superconducting gap Δ . For large ρ_n and small Δ , the shortening of the geometrical length which corresponds to some fixed electrical length on the superconducting microstrip transmission line compared to the normal-conducting state is most pronounced. This shortening becomes less severe when ρ_n becomes smaller and smaller like it is the case in high-quality Al.

In our work we propose microstrip transmission line geometries yielding characteristic impedances of the order of 50Ω or less using a $2 \mu\text{m}$ thick dielectric layer made of SiO_2 , for which we assume a relative permittivity of $\epsilon_r \approx 3.75$. This makes a microstrip transmission line geometry necessary where $W/d > 1$, but which is not much

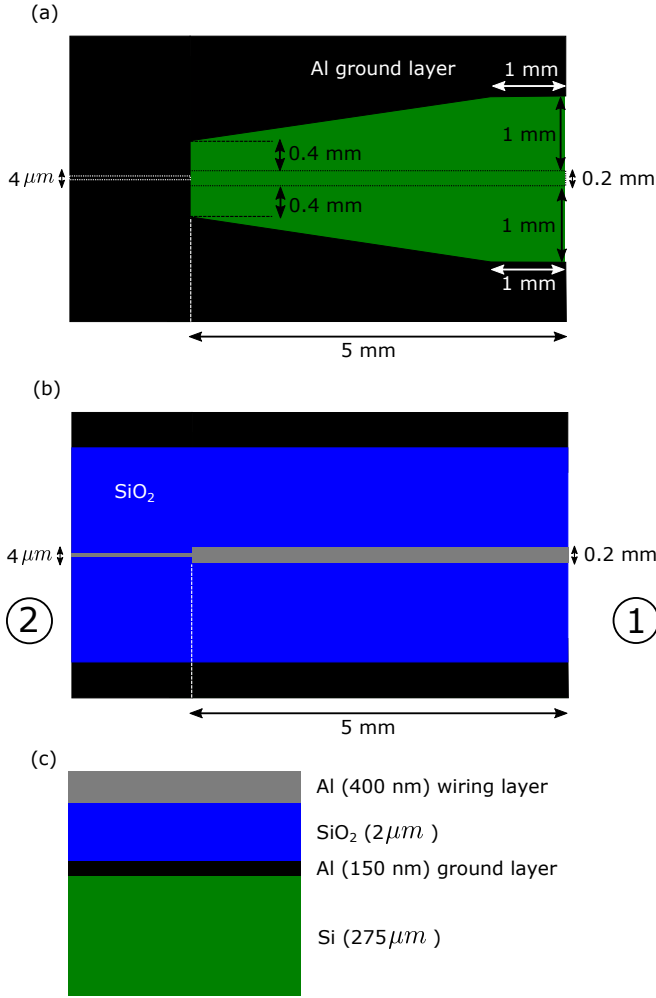


FIG. S3. (a) and (b), dimensions for an ultra broadband dielectric loaded CPW-to-MS transformer where port '2' is the one which could connect to the JPA microstrip circuitry. Both ports '1' and '2' have a characteristic impedance of 50Ω . (a) shows the ground layer and (b) shows the wiring layer on top of a SiO_2 dielectric layer for which we assume a dielectric constant of $\epsilon \approx 3.75$. In (a) we indicate by the dotted lines the dimension and position of the wiring layer shown in (b). (c) Layer stack of the circuit. Note that while the bulk Si handler wafer is also the dielectric for the dielectric loaded CPW, the relevant dielectric layer for the MS circuit is just the SiO_2 layer and for this part of the circuit the fields are confined between the ground (shown in black color) and wiring layer (shown in grey color).

larger than '1', like required for the approximations in the work of Kautz [R. L. Kautz, *J. Appl. Phys.* **49**, 308, (1978)]. Therefore, fringing fields play an increasing role in our case and a conformal mapping calculation keeping higher order terms to obtain more precise values for the capacitive admittance and series impedance per unit length line of the transmission line becomes necessary.

Collin reports such a conformal mapping technique using a similar microstrip geometry liked employed in our design [R. E. Collin, 'Foundations for Microwave Engi-

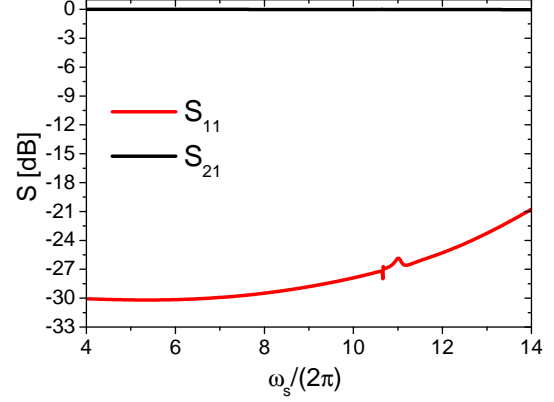


FIG. S4. Simulation results for the circuit shown in Fig. S3. We show the scattering parameters for excitation from port '1' whereas the simulation obtains the same scattering parameters for excitation from port '2' because of the reciprocity of the circuit.

neering', 2nd edition, IEEE Press, Wiley-Interscience]. The theory provided by *Kautz* can then be modified to account for the microstrip transmission line geometries in our device.

The capacitive admittance and series impedance including higher order terms as a result of the conformal mapping calculation reads then:

$$\begin{aligned}
 Y[\omega] &= i\omega\epsilon_0\epsilon_{eff} \left[\frac{W}{d} + 1.393 + 0.667 \ln \left(\frac{W}{d} + 1.444 \right) \right] \\
 Z[\omega] &= i\omega\mu_0 \left[\frac{W}{d} + 1.393 + 0.667 \ln \left(\frac{W}{d} + 1.444 \right) \right]^{-1} \\
 &\quad + \frac{1}{W} (Z_{s,b}[\omega] + Z_{s,w}[\omega]) .
 \end{aligned} \tag{S33}$$

In the above equations ϵ_0 and μ_0 are the free space permittivity and permeability and the effective dielectric constant reads:

$$\begin{aligned}
 \epsilon_{eff} &= \frac{\epsilon_r + 1}{2} + \frac{\epsilon_r - 1}{2} \left(1 + \frac{12d}{W} \right)^{-1/2} \\
 &\quad - 0.217 (\epsilon_r - 1) \frac{t}{\sqrt{Wd}} ,
 \end{aligned} \tag{S34}$$

where t is the thickness of the wiring conductor of the microstrip transmission line. Equations (S33) and (S34) are valid for the case $W > d$. Furthermore, $Z_{s,g}$ and $Z_{s,w}$ are the surface impedances of the ground and wiring layers of the superconducting Al microstrip transmission line. For the latter two quantities and for all practically relevant situations in Al one can assume the local and dirty limit (the magnetic penetration depth is larger or of the order of the coherence length and the coherence length is larger than the electron mean free path), although one has to realize that Al is pretty much at the transition between

the local and dirty limit and the extreme anomalous limit (the magnetic penetration depth is smaller than the coherence length and than the electron mean free path) [D. C. Mattis and J. Bardeen, Phys. Rev. **111**, 412, (1958)]. However, in practice the local and dirty limits account well enough for the experimental observations and greatly simplify the dispersion relation calculations. The expression for the surface impedance in these limits then reads:

$$Z[\omega] = \sqrt{\frac{i\omega\mu_0}{\sigma[\omega]}} \coth\left(\sqrt{i\omega\mu_0\sigma[\omega]}t\right), \quad (\text{S35})$$

where $\sigma[\omega] = \sigma_1[\omega] - i\sigma_2[\omega]$ is the complex conductivity from the Mattis-Bardeen theory [D. C. Mattis and J. Bardeen, Phys. Rev. **111**, 412, (1958)] and t is the conductor thickness of the ground and wiring layers as indicated in Fig. 1(c) of the main text and in Fig. S3(c) of this supplemental information. Equation (S35) depends on the superconducting gap through the complex conductivity [D. C. Mattis and J. Bardeen, Phys. Rev., **111**, 412, (1958)].

The characteristic impedance can then be expressed as usual as:

$$Z_c[\omega] = \sqrt{\frac{Z[\omega]}{Y[\omega]}}, \quad (\text{S36})$$

and the complex propagation constant $\gamma[\omega] = \alpha[\omega] + i\beta[\omega]$ reads:

$$\gamma[\omega] = \sqrt{Z[\omega]Y[\omega]}. \quad (\text{S37})$$

The loss and geometrical length for one wavelength on the transmission line is evaluated as:

$$\begin{aligned} \alpha[\omega] &= \text{Re}(\gamma[\omega]) \\ \lambda[\omega] &= \frac{2\pi}{\text{Im}(\gamma[\omega])}. \end{aligned} \quad (\text{S38})$$

In a final step we compare circuit simulations using CST microwave studio [CST-Computer Simulation Technology, <https://www.cst.com>] from which we obtain the dispersion relation on the superconducting Al microstrip transmission line with the dispersion relation we obtain from the analytical theory we have presented before. In the model we establish in CST, we assume an ultra low loss electrical (normal) conductor for reasons of computational speed and model simplicity. We find that for a low normal-state resistivity of the superconducting Al

material of $0.1 \mu\Omega\text{cm}$, the CST model reproduces the results of the analytical theory (taking superconductivity explicitly into account) up to an uncertainty of 3% for both the characteristic impedance and for the geometrical length corresponding to an electrical length of one wavelength on the superconducting microstrip transmission line. For higher resistivities of say $0.3 \mu\Omega\text{cm}$ and $0.6 \mu\Omega\text{cm}$, the characteristic impedance which we obtain from the same CST model is still in reasonable agreement with the analytical theory. However, the analytical theory yields a geometrical length, corresponding to one wavelength on the superconducting transmission line, which is shorter by 4% and by 6% compared to the normal conducting state (or compared to a superconducting Al conductor with very low normal-state resistivity). In all of these calculations we assume a superconducting gap of $\Delta = 0.182 \text{ meV}$ at 10 mK.

We have observed similar, more severe effects in our earlier works [M. P. Westig et al., J. Appl. Phys. **114**, 124504, (2013); M. P. Westig et al., J. Appl. Phys. **112**, 093919, (2012); M. P. Westig et al., Supercond. Sci. Technol. **24**, 085012, (2011)] using niobium based (and, hence, a material with up to ten times higher normal-state resistivity than in Al) microstrip circuits. Circuits which should employ the disordered superconductors NbN or NbTiN will lead to an even more severe modification of the dispersion relation, resulting in an effective geometric shortening of the transmission line (again with the goal to keep the electrical length constant) of up to 30% because of normal-state resistivities approaching $100 \mu\Omega\text{cm}$ and more.

ADDITIONAL CIRCUIT CHARACTERISTICS

In this section we provide additional circuit characteristics. Figure S5 shows the signal coupling from the embedding circuit to the JJOs being very close to '1' over the entire operation bandwidth of the JPA around 6 GHz. Figure S6 shows the relative phase difference between the ports (2) and (3) of the branch-line coupler. A stable phase relation of $\pi/2$ over the operation bandwidth of the JPA is the basis of the directional signal routing. Finally, Fig. S7 shows the effect of relatively detuned SQUIDs on the signal routing and return loss, adding a phase difference to the amplified signals additional to the one imposed by the branch-line coupler.

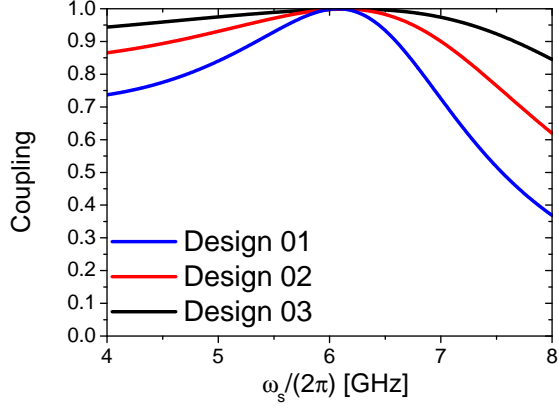


FIG. S5. Coupling from the embedding circuit to the Josephson junction oscillators referred to the point where we specify Y_{in}''' in Fig. 1(a). For all three designs, the coupling is between '1' and '0.95'.

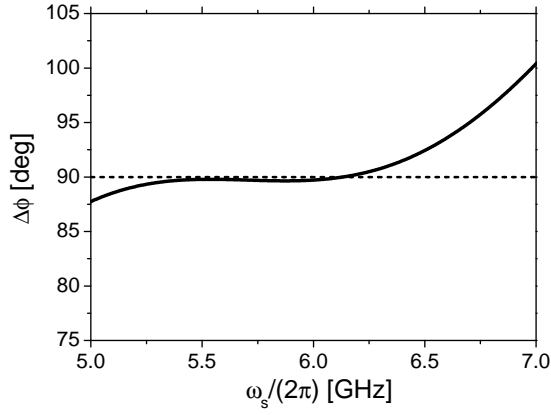


FIG. S6. Relative phase difference between the ports (2) and (3) of the branch-line coupler in the JPA circuit.

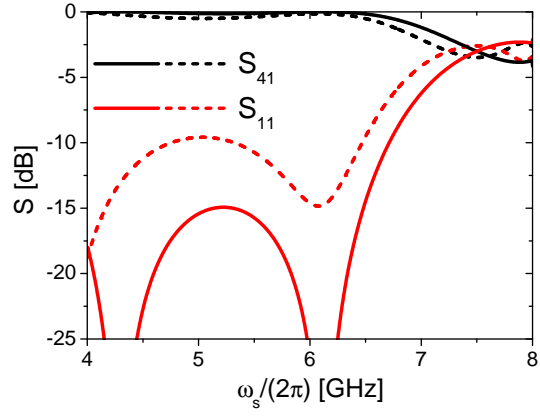


FIG. S7. Degraded directivity S_{41} and return loss S_{11} as a result of relatively detuned SQUIDS, resulting in different plasma frequencies ω_0 . The incident signals which are amplified and reflected from the individual nonlinear JJOs shown in Fig. 1(a) will obtain different phases due to this detuning. The figure summarizes the effect of a rather large additional phase difference of $\pi/18$ between the two nonlinear JJOs shown as dashed lines, compared to the ideal case with equal tuned SQUIDS shown as solid lines.